Dominant modes of Diurnal Temperature Range variability over Europe and their relationships with large-scale atmospheric circulation and sea surface temperature anomaly patterns

M. Ionita (1), G. Lohmann (1), N. Rimbu (1,2,3) and P. Scholz (1)

(1) Alfred Wegener Institute for Polar and Marine Research, Bremerhaven, Germany

(2) University of Bucharest, Faculty of Physics, Bucharest, Romania

(3) Climed Norad, Bucharest, Romania

Corresponding author:

Dr. Monica Ionita

Alfred Wegener Institute for Polar and Marine Research

Paleoclimate Dynamics Group
Bussestrasse 24 (Room A-111)
D-27570 Bremerhaven Germany

Tel +49 -471 4831 1883

e-mail: Monica.Ionita@awi.de

Abstract

The relationships between the dominant modes of interannual variability of Diurnal Temperature Range (DTR) over Europe and large-scale atmospheric circulation and sea surface temperature anomaly fields are investigated through statistical analysis of observed and reanalysis data. It is shown that the dominant DTR modes as well as their relationship with large-scale atmospheric circulation and sea surface temperature anomaly fields are specific for each season.

During winter the first and second modes of interannual DTR variability are strongly related with the North Atlantic Oscillation and the Scandinavian pattern, while the third mode is related with the Atlantic Multidecadal Oscillation. Strong influence of the Atlantic Multidecadal Oscillation and the Arctic Oscillation on spring DTR modes of variability was also detected. During summer the DTR variability is influenced mostly by a blocking-like pattern over Europe, while the autumn DTR variability is associated with a wave-train like pattern, which develops over the Atlantic Ocean and extends up to Siberia. It is also found that the response of DTR to global sea surface temperature is much weaker in spring and summer comparing to winter and autumn. A correlation analysis reveals a strong relationship between DTR modes of variability and the Cloud Cover anomalies during all seasons. The influence of the potential evapotranspiration and precipitation anomalies on DTR modes of variability is strongest during summer, but it is significant also in spring and autumn. It is suggested that a large part of interannual to decadal DTR variability over Europe is induced by the large-scale climate anomaly patterns via modulation of cloud cover, precipitation and potential evapotranspiration anomaly fields.

1. Introduction

The latest report of the Intergovernmental Panel on Climate Change (IPCC) presents a consensual view on global warming (Trenberth et al., 2007). According to this report *"the global mean surface temperatures have risen by 0.74°C +/- 0.18°C over the last 100 years"*. Much of this warming has involved a faster rise in the daily minimum temperatures than in the daily maximum temperatures (Easterling et al., 1997). This led, over large parts of the world, to a decreasing trend in the Diurnal Temperature Range (DTR).

During the second part of the twentieth century the diurnal temperature range (DTR) or difference between daytime and nighttime temperature, has been reduced on a global basis by 0.1°C per decade. Nevertheless, several regions do not follow the planetary pattern – among them, eastern North America, middle Canada, portions of Europe, parts of Southern Africa, India, Nepal, Japan, New Zealand, the western tropical Pacific Islands, Australia and Antarctica display no change or a slight increase of the day–night temperature differences (Karl et al., 1994; Horton, 1995; Brunet et al., 2001c, Böhm and Auer, 1994; Brázdil et al., 1994; Kaas and Frich, 1995, Makowski et al., 2009, Makovski et al., 2008). Over Europe, Makovski et al. (2008) found that DTR has significantly increased since the early 1980s, which contradicts the general idea that DTR is decreasing (Easterling et al., 1997; Vose et al., 2005). Klok and Tank (2009) using 333 stations covering most of Europe, for the period 1960 – 2000, found that DTR shows a strong positive trend during spring and summer, a negative trend during winter and almost no trend for autumn.

Concurrently, an increase in the cloudiness has also been observed over some of the same regions (Dobesch, 1992; Jones, 1991; Weber, 1990; Noris et al., 1998; Norris and Wild, 2007, Henderson-Sellers, 1992) and it has been suggested that these two phenomenon, i.e.

decreasing in DTR and increasing cloudiness, may be related (Michaels and Stooksbury, 1992; Plantico et al., 1990; Zhou et al., 2007). Increased clouds and precipitation normally decrease the diurnal temperature range (DTR) and thus have commonly been offered as an explanation for the trend of reduced DTR observed for many land areas over the last several decades.

An increase in global temperatures is very likely reflected in precipitation and atmospheric moisture, via induced changes in the atmospheric circulation, a more active hydrological cycle, an increase in the water vapor holding capacity throughout the atmosphere (Folland et al., 2001) and changes in the leading modes of interannual variability, e.g. El Niño – Southern Oscillation, the Arctic Oscillation and the North Atlantic Oscillation.

Variations in the diurnal temperature range (DTR) tend to occur as a result of the variations in the surface radiative, latent and sensible heat fluxes. Since 1950, minimum temperature increased about twice as fast as maximum temperature, which led to a broad decline in DTR (Folland et al., 2001). Changes in the cloud cover, precipitation, soil moisture and atmospheric circulation can be responsible for much of this declining trend (Dai et al., 1999; Przybylak, 2000; Braganza et al., 2004).

The atmospheric circulation can influence DTR by influencing the boundary layer structure, cloudiness and snow cover, depending on the season. During the second half of the 20th century the atmospheric circulation has experienced large variations and shifts (Mantua et al., 1997; Thomson and Wallace, 1998; Philipp et al., 2007). We hypothesize that these variations can have also a strong influence on both interannual and long-term trend of the DTR.

The impact of large-scale circulation on the mean temperature over Europe has been described in many previous studies (e.g. Hurrell, 1996; Osborn et al., 1999; Zverayev et al., 2009). Trigo et al. (2002) emphasized the influence of the North Atlantic Oscillation (NAO)

on the variability on maximum temperature and minimum temperature fields, but their study was limited to the winter season. Over Europe DTR was found to be strongly related to the surface solar radiation, both on annual scale as well as on seasonal scale, this relationship being modulated by synoptic scale pressure systems (Makovski et al., 2009). However, to our knowledge, a separate analysis of the seasonal variability of DTR and its relationship with the large-scale atmospheric circulation and global SST has not yet been undertaken.

Motivated by these findings, we focus on a systematic evaluation of DTR variations over Europe on seasonal time scales. Taking this into account, the main goals of this study are: i) to quantitatively describe the leading modes of DTR variability over Europe on a seasonal time scale and ii) to determine to what extent the changes induced by the atmospheric circulation and global sea surface temperature account for the DTR variability over Europe. Employing the composite and correlation maps, patterns of 500mb geopotential height (G500), global sea surface temperature (SST), precipitation (PP), cloud cover (CLD) and potential evapotranspiration (PET) are used to explain the DTR variability. The configuration of these patterns can provide information on the mechanism by which the atmospheric circulation can influence the regional DTR.

This paper is organized as follows: the data sets used in this study and the methods employed are described in section 2. The spatio-temporal variability of DTR, on a seasonal time scale, is presented in section 3. The relationship between the leading modes of DTR and the northern hemisphere atmospheric circulation, global sea surface temperature and precipitation, cloud cover and potential evapotranspiration is examined in section 4 and 5, respectively. Finally, the concluding remarks and discussion are presented in section 6.

2. Data and methods

For DTR we used the gridded data set CRU TS3.1 from the Climatic Research Unit (CRU) of the University of East Anglia (Mitchell and Jones, 2005). This data set provides monthly values for various parameters for the global land areas, including diurnal temperature range. The temporal coverage is 1901 – 2008 on a 0.5° x 0.5° grid. The DTR includes information from individual records of daily temperature minima (Tmin) and maxima (Tmax). Precipitation, cloud cover and potential evapotranspiration data were extracted from the same data set (CRU TS3.1) for the period 1901 – 2008.

To investigate the relationship of DTR with global sea surface temperature we use the Hadley Centre Sea Ice and Sea Surface Temperature data set (HadISST, Rayner et al., 2003). This data set covers the period 1901 – 2008.

For the Northern Hemisphere atmospheric circulation we used Monthly Sea Level Pressure (SLP) on a 2ºx2º grid from Twentieth Century Reanalysis (V2) data and Geopotential Height at 500mb (Compo et al., 2011; Compo et al., 2006; Whitaker et al., 2004), for the period 1901-2008.

We also used the time series of the monthly teleconnection indices described in Table 1. From the monthly time series we computed the seasonal means, by averaging the months December/January/February (DJF), March/April/May (MAM), June/July/August (JJA) and September/October/December (SON). The time series were detrended and normalized by their corresponding standard deviation.

In order to analyze the temporal structure (interannual and decadal variability) of the DTR variability the wavelet power spectrum analysis was used. The wavelet analysis used in this paper follows the methods of Torence and Compo (1998). Statistical significance is

determined against a red noise null hypothesis using a chi-squared test. By decomposing a time series into a time-frequency space, it is possible to determine the dominant modes of variability, as well as, how these modes vary in time.

The wavelet transform is designed to analyze time series that contain non-stationary power over many different frequency scales (Daubechies, 1990). The *wavelet transform* breaks up a signal into scaled versions of a *wavelet function*, where the scale of the wavelet (the window) varies with frequency. Thus, the wavelet is narrow in time at high frequencies and the scale of the wavelet increases with decreasing frequency. The wavelet transform, therefore, expresses a time series in three-dimensional space: time (x), scale/frequency (y), and power (z).

The dominant patterns of variability in the DTR are based on Empirical Orthogonal Function (EOF) analysis (e.g. von Storch and Zwiers, 1999). EOF technique aims at finding a new set of variables that captures most of the observed variance from the data through a linear combination of the original variables. The EOF analysis provides a convenient method for studying the spatial and temporal variability of time series which cover large areas. This method splits the temporal variance of the data into orthogonal spatial patterns called empirical eigenvectors. In this study the EOF is applied to the detrended and standardized anomalies of the seasonal DTR. For all seasons we retained just the first three leading modes.

3. Leading modes of spatio-temporal DTR variability and their relationship with atmospheric teleconnection patterns

3.1 Winter

The first leading mode for winter DTR (Figure 1a), which describes 25.5% of the total variance, has a dipole like structure between the southern part of Europe and the central and northern part. The highest loadings are observed over the Baltics and central European Russia (Figure 1a). The negative loadings in the southern part of Europe are much smaller than the positive loadings. The corresponding principal component (PC1) presents pronounced interannual and decadal variability (Figure 1d) and is negatively correlated with the winter NAO index (r = -0.49, 99% significance level). Wavelet analysis emphasizes enhanced variability in the 7-9 years band and in the decadal band at around 60 years (Figure 1g). Also NAO shows enhanced variability at 7 – 9 years scale.

The second winter EOF (Figure 1b), explaining 9.1% of the total variance, has a dipole structure, with positive loadings over the central part of Europe and negative loadings over northeastern Europe. The corresponding principal component (PC2) presents a multidecadal variability component, which can be inferred both from evolution of PC2 in time as well as from the wavelet analysis (Figure 1e,h). PC2 (Figure 1e) is significantly correlated (r=-0.62, significant at 99% level) with the Scandinavian teleconnection pattern (Barnston and Livezey, 1987). The Scandinavian pattern (SCA) consists of a primary circulation centre over Scandinavia and two weaker centers of opposite sign over Western Europe and eastern Russia/ western Mongolia. The Scandinavian pattern has been previously referred to as the Eurasia-1 pattern by Barnston and Livezey (1987). The positive phase of the Scandinavian

pattern is associated with below-average temperatures across central Russia and above-average precipitation across central and southern Europe.

The third winter EOF (7.1% explained variance) has also a dipole structure (Figure 1c) with positive loadings over the central part of the Scandinavian Peninsula and negative loadings over the central part of Russia. Outside these regions the loadings are close to zero. PC3 (Figure 1f) presents a decadal component in the 30-35 years band as well as a decadal component in the 60 years band (Figure 1i). The periodicity in the 30-35 years band can be associated with the Bruckner cycle (Brückner, 1890), which was related to variations in the length of the sunspot cycles (Wang et al., 2000). This cycle has also been found in temperature reconstructions in the northern Fennoscandinavia (Briffa et al., 1992). The peak in the 60 years band can be related to the Atlantic Multidecadal Oscillation (AMO), which is known to have an enhanced variability in this band (Enfield et al., 2001). Overlaid over the time series of PC3 (Figure 1f) is the winter AMO index. The correlation coefficient, after applying a 7 year running mean to both time series (PC2 and AMO) is r = -0.61 (significant at 99% level). The two time series fit quite well each to other, not only on multidecadal time scales, but also for inter-annual variability. AMO is associated with basin-wide SST and SLP fluctuations. The positive AMO phase is characterized by an almost uniform warming of the North Atlantic (Enfield et al., 2001). The AMO warm phase between 1950s to early 1960s is associated with high DTR anomalies, while the cold phase from the beginning of 1970s up to 1990s is associated with relatively low DTR anomalies.

3.2 Spring

The first spring EOF pattern (Figure 2a), which explains 18.5% of the total variance, is characterized by high and positive loadings over their central part of the Scandinavian

Peninsula, Poland and the western part of Russia and negative loadings over the southernmost part of Europe. The corresponding time series (PC1 MAM) is characterized by a pronounced multidecadal band (Figure 2d), at around 60 years, which might be related to the influence of AMO over the temperature variability in Europe. PC1 MAM presents also a strong inter-annual variability (Figure 2g).

The second EOF (15.2% of the total variance) shows a dipole between the Scandinavian Peninsula and the north-western part of Russia and the rest of Europe (Figure 2b). The highest loadings are centered over parts of Russia (negative loadings), while the high positive loadings are centered over the Balkans. PC2 MAM (Figure 2e,h) shows both inter-annual variability and decadal (~30 years) to multidecadal variability (~60 years). Spring PC2 is positively correlated with the spring Arctic Oscillation (AO) index. The correlation coefficient between the two time series is r=0.41 (significant at 99% level). AO is the dominant mode of variability on interannual time scales in the Northern Hemisphere (Thomson and Wallace, 1998) and exhibits an annular pattern with decreased SLP over the Arctic basin associated with increased SLP at midlatitudes with centers of action in the North Atlantic and North Pacific. In the positive phase higher pressure at midlatitudes drives ocean storms farther north, and changes in the circulation pattern bring wetter conditions to Alaska, Scotland and Scandinavia, as well as drier conditions to the western United States and the Mediterranean region.

EOF 3 (Figure 2c), explaining 8.7% of the total variance, emphasizes a dipole-like structure between the eastern part of Europe and Russia (negative loadings) and the western part of Europe. Spring PC3 presents both inter-annual as well as decadal variability (Figure 2f,i). From the wavelet spectrum of the first three spring PCs we can infer that also spring temperature variability can be modulated by the multidecadal variability in the Atlantic basin, via the Atlantic Multidecadal Oscillation.

3.3 Summer

Summer EOF1 (19.6% of the total variance) (Figure 3a) emphasizes a north-south dipole between the Scandinavian Peninsula and the northern part of Europe (negative loadings) and the southern part of Europe (positive loadings). The corresponding principal component (PC1) shows pronounced decadal to multidecadal variability (Figure 3d). PC1 is dominated by a decadal component in the 30-35 years band. Also the 60 years component is present in the wavelet of PC1 (Figure 3g). As in the case of winter, the Scandinavian teleconnection pattern affects part of the DTR variability also in summer. The time series of summer PC1 is positively correlated to the summer Scandinavian teleconnection pattern. The correlation coefficient between the two time series (PC1 and SCA) is 0.60 (significant at 99% level).

The second EOF (Figure 3b), which explains 11.3% of the total variance, shows strong positive loadings over Eastern Europe and strong negative loadings over the central part of the Scandinavian Peninsula. Summer PC2 shows both inter-annual to multidecadal variability (Figure 3e,h).

Summer EOF3 (Figure 3c), explaining 8.9% of the total variance, is characterized by positive loadings over France and Germany and negative loadings over Russia. PC3 shows a strong peak in the 7-9 years band (Figure 3f,i).

3.4 Autumn

During autumn the first EOF mode (Figure 4a) accounts for 15.2% of the total variance of DTR. The spatial pattern of this mode is characterized by positive loadings over the Baltic Sea realm and negative loadings in the southern part of Europe. SON PC1 (Figure 4d,g)

shows enhanced multidecadal variability until the beginning of 1960s PC1, after this period the time series being characterized mainly by the inter-annual variability.

The second EOF mode (Figure 4b) of autumn DTR variability explains 12.0% of the total variance. Structurally, this pattern resembles the second EOF mode of summer, but autumn EOF2 presents higher negative loadings over France and Scandinavian Peninsula and positive loadings over central Russia. The wavelet spectrum of PC2 (Figure 4e,h) shows significant peak in the 4-8 years band.

The third EOF for autumn season (Figure 4c), explaining 8.9% of the total variance, is characterized by negative loadings over the north-eastern part of the Scandinavian Peninsula and positive loadings over France and Germany. Outside these regions the loadings are close to zero. Notably, SON PC3 shows an upward trend until 1960s (Figure 4f). The wavelet spectrum (Figure 4i) shows some variability in the 1-4 years band after the beginning of 1960s. PC3 is positively correlated with autumn NAO index (r = 0.36).

4. Relationship with large-scale atmospheric circulation and global SST

To identify the physical mechanism responsible for the connection between DTR seasonal variability and large-scale atmospheric circulation and global SST, we constructed the composite maps between the first three principal components, for each season, and G500 and global SST for the years of high (> 1), respectively low (<-1) values of the normalized times series of the PCs. The years that were used for the composite maps are shown in table 2, for each time series and each season. This threshold was chosen as a compromise between the strength of the climate anomalies associated to flow anomalies and the number of maps

which satisfy this criteria. Further analysis has shown that the results are not sensitive to the exact threshold value used for our composite analysis (not shown).

4.1 Winter

Figure 5 shows the composite maps between the leading winter PCs and the winter G500 (left graphs) and winter global SST (right graphs). High values of PC1 are associated with a wave train in the G500 field (Figure 5a), similar to the western Atlantic Pattern identified by Wallace and Gutzler (1981). The western Atlantic Pattern is reminiscent of NAO, but exerts a strong influence over the Eurasian continent, due to the center situated over Siberia. This pattern (negative G500 anomalies over the Atlantic Ocean and Siberia and positive G500 anomalies over the north Atlantic and China) is associated with a weak jet stream over the western Atlantic and a weaker-than-normal Icelandic Low and Azores High. The SST composite map (Figure 5d) resembles the SST pattern associated with the negative NAO pattern.

The G500 composite map for winter PC2 (Figure 5b) is characterized by a center of positive G500 anomalies over the central part of Europe (low cloudiness), a center of negative G500 anomalies over Greenland which extends up to Scandinavia (high cloudiness) and another center of positive anomalies (low cloudiness) which extends from Siberia to the western part of the Pacific Ocean. This pattern is responsible for the advection of cold air from Greenland towards Scandinavia and the western part of Russia and humid air from the ocean towards the central part of Europe. This pattern resembles the negative phase of the Scandinavian (SCA) teleconnection pattern (Barnston and Livezey, 1987). The negative phase of SCA is associated with above average temperatures over central Russia and above-average precipitation across central and southern Europe, and below-average precipitation across

Scandinavia, in agreement with winter EOF2 pattern (Figure 2b). The strong relationship between PC2 and SCA was identified also in the previous section. The SST composite map (Figure 2e) is characterized by positive SST anomalies over the North Atlantic basin that extends from the Gulf of Mexico until the European coast.

The composite map of the third principal component (PC3) and winter G500 (Figure 5c) shows a dipole-like structure between the Scandinavian Peninsula and Barents Sea (negative G500 anomalies) and the southern part of Europe and Siberia (positive G500 anomalies). The main characteristic of the composite map between PC3 and global winter SST (Figure 5f) is the quasi-monopolar SST anomalies in the North Atlantic Ocean. As indicated by other studies (Latif et al., 2004; Knight et al. 2005) such a quasi-monopolar structure is associated with the extreme phases of the Atlantic Multidecadal Oscillation (AMO). High (low) SST anomalies over the North Atlantic are associated with positive (negative) phase of AMO. According to Figure 5f, low PC3 values are occurring during the positive phase of AMO.

4.2 Spring

The composite map between MAM PC1 and spring G500 (Figure 6a) is characterized by a tripole-like pattern with a center of negative G500 anomalies over the eastern Atlantic Ocean, a center of positive G500 anomalies over the British Isles and Scandinavia and another center of negative anomalies over Siberia. High values of spring PC1 are accompanied by positive SST anomalies over the North Seas and the Mediterranean Sea (Figure 6d).

The composite map between MAM PC2 and G500 (Figure 6b) resembles the positive phase of the Arctic Oscillation. As shown in previous paragraph, PC2 and MAM AO index are significantly correlated, implying the around 15% (the explained variance of MAM EOF2) of

the spring DTR variability can be explained by AO. The SST composite (Figure 6e) is characterized by a tripole-like pattern, with altering signs of SST anomalies in the Atlantic, similar to those corresponding to the positive phase of AO. The positive phase of AO is characterized by above average temperatures over Scandinavia and Russia and below average temperatures over the southern part of Europe, which is in agreement with the second EOF structure for spring (Figure 2b).

The composite map between MAM PC3 and spring G500 (Figure 6c) is associated with a jet-guide which starts over the eastern coast of U.S. and extends up to Eurasia. A similar jet-guide was identified by Hoskins and Ambrizzi (1993). According to them, putting a forcing in the vicinity of the North Atlantic jet-stream maximum will produce a propagating wave train in the North Atlantic jet up to Eurasia. The anticyclonic circulation over the British Isles and central Europe is consistent with a divergent zone and positive DTR anomalies, while the cyclonic circulation over western Russia and south-eastern part of Europe is consistent with negative DTR anomalies over these regions. The SST composite (Figure 6f) is consistent with the G500 pattern with alternant anomalies over the Atlantic basin.

4.3 Summer

The composite map between summer PC1 and summer G500 (Figure 7a) is associated with a center of negative G500 anomalies over the Mediterranean region and southern Europe and a center of positive G500 anomalies over Scandinavia and the British Isles. This kind of pattern favors north-easterly winds which carry cold air from the north and enhances convergence over the Mediterranean region. This pattern resembles the positive phase of summer SCA. In concordance with G500 anomalies, positive PC1 anomalies are associated with positive SST

anomalies (Figure 7d) over the North Sea and negative SST anomalies on the south coast of Greenland.

Positive JJA PC2 anomalies are associated with a blocking-like pattern (Figure 7b), which yields a cyclonic circulation which extends from Iceland until the Scandinavian Peninsula, an anticyclonic circulation over most of the European region and a cyclonic circulation over the Caspian Sea. This kind of pattern is usually associated with European droughts and heat waves (Cassou et al., 2005; Fisher et al., 2007a). The composite map between PC2 and summer SST is shown in Figure 7e. The SST composite map is chraterized by a quasi-monopolar structure in the North Atlantic with positive SST anomalies over the entire North Atlantic. As described in Fugure 5f, such a quasi-monopolar structure is associated with the extreme phases of the Atlantic Multidecadal Oscillation (Mesta-Nuñez and Enfield, 1999). The summer DTR PC2 time series is strongly related with SST anomalies over the whole basin. This structure is consistent with the strong correlation found between PC2 and summer AMO index ($r = 0.59$, significant at 99% level).

The composite map between JJA PC3 and G500 field (Figure 7c) is similar to the composite map between MAM PC3 and G500 (Figure 6c), implying a recurring and persistent pattern from spring to summer. The map resembles a stationary wave pattern with anomalously low G500 over the central North Atlantic, positive G500 anomalies over the Western Europe and the British Isles and negative G500 anomalies over the Eastern Europe. This pattern is responsible for positive DTR anomalies over the Western Europe and negative DTR anomalies over the Eastern Europe and Russia. The wavetrain in the G500 filed is accompanied by strong negative SST anomalies in the northern part of the Atlantic Ocean (Figure 7f) and positive SST anomalies over the European coast.

4.4 Autumn

The composite map between SON PC1 and autumn G500 field is characterized by a wave train of altering signs (Figure 8a), with a cyclonic circulation over the central Atlantic, an anticyclonic circulation over the British Isles and north-western part of Europe, a cyclonic circulation over Russia and Barents Sea and an anticyclonic circulation over China. In autumn, positive PC1 anomalies are associated with a divergent zone over central and southern part of Europe (positive G500 anomalies) and positive SST anomalies (Figure 8d) over the European coast and North Sea and negative SST anomalies in the north-western part of the Atlantic Ocean.

Positive DTR anomalies, in terms of SON PC2, occur under a strong anticyclonic circulation over the western part of the North Atlantic Ocean, a cyclonic circulation over the northern part of the Atlantic Ocean and the British Isles and an anticyclonic circulation over the eastern part of Europe (Figure 8b). The corresponding SST composite map (Figure 8e) is characterized by negative SST anomalies on the western coast of the British Isles and positive SST anomalies over the central North Atlantic.

Positive anomalies of the third autumn principal component (PC3) are associated with positive G500 anomalies over the Atlantic Ocean extending up to the western part of Europe and a center of negative G500 anomalies over Greenland and the Scandinavian Peninsula (Figure 8c). This pattern resembles the positive phase of the North Atlantic Oscillation. Positive PC3 anomalies are associated with positive SST anomalies over the European coast and the Mediterranean Sea (Figure 8f).

5. Relationship with precipitation, cloud cover and potential evapotranspiration

In this section the relationship between the seasonal DTR and precipitation, cloud cover and potential evapotranspiration is analyzed in terms of correlation maps between the first three PCs for each season and the PP, CLD and PET fields. Dai et al. (1997) found a strong relationship between precipitation and DTR. Dai et al. (1999) suggested that up to 80% of the DTR variance can be explained by the combination of precipitation and clouds. Precipitation can decrease DTR through evaporative cooling, especially during the day when the potential evapotranspiration is higher and when the maximum temperature is more sensitive to water availability than the minimum temperature (Mitchell et al., 1995). An increase in the total cloud cover can be seen as a possible cause for the decreasing DTR (Karl et al., 1993; 1994; Saltzman and Pollack, 1997). Clouds can limit the amount of net radiation at the surface and inhibit the rise of the surface air temperature. According to Dai et al. (1999) cloudy days can reduce DTR by 25-50%, compared to clear sky days.

5.1 Winter

Figure 9 shows the correlation map between PC1 corresponding to the first EOF mode of winter and seasonally averaged winter PP (Figure 9a), CLD (Figure 9d) and PET (Figure 9g). The highest negative correlations are found with the CLD field (values up to -0.8), especially over the central and northern part of Europe, following the pattern of EOF1. PET plays a less important role in driving the variability of DTR in winter. The correlation map between PC of the second winter EOF mode and winter PP, CLD and PET fields are depicted in Figure 9b, e

and h, respectively. The correlation maps emphasize a dipole like structure between the northern part of Europe (positive correlations) and the southern part of Europe (negative correlations). As in the case of PC1 the highest correlations are found with the CLD field. In the case of winter PC3 the correlation map with winter PP and CLD shows strong positive correlation over eastern Europe and negative correlation with CLD filed over Scandinavian Peninsula and western Europe. The correlation between PC3 and PET are very small and insignificant.

The dominant EOF pattern of DTR in winter (Figure 1a) has a spatial structure similar to the correlation map of PC1 and CLD field (Figure 9d). Positive (negative) DTR anomalies are associated to negative (positive) CLD anomalies in almost all grid points in the considered domain. In contrast, positive or negative PP or PET anomalies are associated both to positive and negative DTR anomalies (Figure 9a,g). For example, positive DTR anomalies are associated with negative PP anomalies over most of the Scandinavian region, but with positive PP anomalies in the northeastern part of the Black Sea (Figure 9a,g). The same apply for the secod (Figure 1b) and third (Figure 1c) EOF patterns as shown by the corresponding correlation maps (Figure 9b,c). The PET anomalies could also lead to DTR anomalies of the opposite sign. Positive DTR anomalies are associated with positive PET anomalies over northern Scandinavia, but with negative PET anomalies over central Europe (Figure 9g). Therefore the patterns of DTR variability (Figure 1a,b,c) are the result of complex large-scale and regional forcing factors which explain also their variability at different time scales (Figure 1d,e,f).

5.2 Spring

In spring the first PC is strongly correlated (up to -0.7) with the CLD field (Figure 10b), especially over the north-eastern part of Europe. There is an out-of-phase relationship between PC1 and the PP and CLD fields. In the same time, the correlation with the PET field is also significant (Figure 10g). The highest correlations are found over the north-eastern part of Europe for all the fields. The correlation maps follow the structure of spring EOF1. Correlations between PC of the second spring EOF and spring PP, CLD and PET are shown in Figure 10b,e and h, respectively. The correlations form a north-south oriented dipole with the largest negative (positive) correlations over the southern part of Europe (northen Europe) for PP and CLD and positive (negative) correlations for PET. The highest correlations are found between PC2 and CLD field. Spring PC3 shows the highest positive (negative) correlations with spring PET (Figure 10i) over western Europe (eastern Europe). The correlation between spring PC3 and PP (Figure 10c) and CLD (Figure 10f) are also significant, but they are smaller than for PET.

The PP (Figure 10a), CLD (Figure 10b) and PET (Figure 10c) patterns associated to the dominant pattern of DTR variability in spring (Figure 2a) have similar spatial structures. Positive (negative) DTR anomalies are related to negative (positive) PP and CLD anomalies as well as with positive (negative) PET anomalies in allmost all grid points of the considered domain. A similar relationship is found for the secod EOF pattern (Figure 2b) and the third one (Figure 2c) as shown by the corresponding correlation maps (Figure 10b,e,h and Figure 10c,f,i, respectively). Because the DTR patterns are dominanted by decadal variations (Figure 2d,e,f), the regional processes play probably a secondary role, so that the usuall relationhip between DTR and these variables, i.e. positive (negative) DTR anomalies correspond to negative (positive) PP and CLD and positive (negative) PET anomalies, prevail.

5.3 Summer

Figure 11a,d,g displays the correlation maps between PC of the first EOF mode of summer DTR and seasonally averaged PP, CLD and PET, respectively. The correlations form a dipole-like structure, with the largest negative (positive) correlations over the northern Europe for PP and CLD (PET). The highest correlations are found between summer PC1 and PET and reach values up to 1 over northern Europe. For summer PC2 the highest negative (positive) correlations are found over the eastern Europe for PP (Figure 11b) and CLD (Figure 11e) (PET (Figure 11h)). The correlations are stronger between summer PC2 and CLD and PET. Summer PC3 shows the highest negative (positive) correlations over the western part of Europe with PP (Figure 11c) and CLD (Figure 11f) (PET (Figure 11i)). The correlation with PET reaches values up to 1 over the western part of Europe.

The dominant EOF patterns of summer DTR variability (Figure 3a,b,c) have spatial structures similar to the corresponding associated correlation maps of PP, CLD and PET (Figure 11). Therefore positive (negative) PP and CLD and negative (positive) PET anomalies lead to positive (negative) DTR anomalies over most of the sub regions of the domain considered in our analysis. Due to the fact that the time coefficients of DTR patterns are dominated by decadal variations (Figure 3 d,e,f) it is possible that this relationship characterizes also the decadal variations of DTR. More complex relationships between DTR and PP, CLD and PET could characterize the interannual or shorter time scales.

5.4 Autumn

Figure 12a,d and e depicts the correlation maps between autumn PC1 and PP, CLD and PET, respectively. The patterns show major centers of negative (positive) correlations over central

and eastern Europe with PP and CLD (PET). The highest correlations are found, as in the case of spring and summer, with CLD and PET. Autumn PC2 is negatively (positively) correlated with PP (Figure 12b) and CLD (Figure 12e) (PET (Figure 12h)) over the eastern part of Europe. The correlations are much higher for CLD and PET than in the case of PP. Correlations between PC of the third mode of fall DTR and seasonally averaged PP, CLD and PET are depicted in Figure 12c, f and i, respectively. The largest negative (positive) correlations are detected over the central part of Europe (northern Europe) with PP and CLD. In the case of PET the values of the correlations with fall PC3 are significant just over the central Europe.

In general, the relationship between the PP, CLD and PET anomalies and DTR obtained for summer, that is negative (positive) PP and CLD and negative (positive) PET anomalies lead to positive (negative) DTR anomalies, is valid also for autumn. Note that also in autumn the time coefficients (PCs) associated to these patterns are dominated by the decadal variability (Figure 4d,e,f). However this relationship is not valid in all sub regions of the analyzed domain. For example, over northern Scandinavia, positive PP and PET anomalies (Figure 12 a,g) are associated with positive DTR anomalies (Figure 4a). In this case the regional processes seem to play a major role in generating DTR anomalies.

6. Conclusions

Several studies tried to determine the controlling factors of DTR (Dai et al., 1999, 2001; Stone and Weaver, 2002, 2003) at interannual to decadal time scales. It is believed that DTR responds strongly to changes in the cloud cover and soil moisture, throughout the effect of evaporative cooling (Dai et al., 1999; Stone and Weaver, 2003).

There are relatively few studies that assess the possible influence of the large-scale atmospheric circulation on the DTR variability. Easterling et al. (1997) showed that an index of surface westerlies is negatively correlated with the DTR over the northern Europe extending to Russia. Przybylak (2000) showed that DTR over the Arctic region is modulated by the atmospheric circulation, via six different synoptic patterns. Over Russia, Razuvaev et al. (1995) suggested that a decrease of DTR in the cold season (November - March) over the northern and central parts, between 1961 and 1990, may have been caused by an increase in the frequency of synoptic situations that favor warm advection and cyclogenesis. Although there are several studies dealing with the analysis on the trends in DTR (Karl et al., 1993; Vose et al., 2005; Dai et al., 1997, 1999), to our knowledge, there is no direct study which treats the DTR variability over Europe in relationship with the atmospheric circulation at a hemispheric scale.

In this study, the relationship among DTR variability and the atmospheric circulation and global SST has been investigated, with a special emphasis on the seasonality of DTR variability. The spatio-temporal variability of seasonal DTR over Europe and the influence of large scale atmospheric circulation and SST on the DTR have been examined by means of EOF and composite and correlation analysis. In order to characterize the atmospheric circulation, 500-hPa geopotential height, precipitation, cloud cover and potential evapotranspiration has been used, for the period 1901-2008. For the same period, DTR seasonal means over Europe have been considered. It is well know that the atmospheric circulation is the main driver of the inter-annual variability of European land surface temperatures, and its influence depends on the season. That is why an index like the "classical" NAO index, whose definition remains the same for all seasons, poorly explains the seasonal temperature anomalies, except winter.

The main conclusions of our study are summarized as follows.

(1) We find that the leading modes of seasonal mean DTR are clearly season-dependent. Although the first EOF patterns, for all seasons, look almost similar, their temporal evolution (in terms of principal components) differ significantly from one season to another. Furthermore, the leading modes of seasonal DTR variability are clearly associated with quite different regimes of the atmospheric circulation.

(2) Through composite and correlation analysis, we show that atmospheric circulation and global SST play a significant role in the interannual variability of seasonal DTR. During winter the variability of DTR is connected to well-known climate modes: NAO, SCA and AMO. The winter PCs are associated with an anticyclonic (cyclonic) circulation over the regions where the corresponding EOF patterns have positive (negative) loadings. During winter the cyclonic circulation is associated with intense precipitation and cloudy days, which in turn can influence Tmax and Tmin and hence DTR. Winter DTR was found to be more correlated with winter Tmin (not shown). For the winter season, the highest correlations were found with the CLD field, for all the PCs analyzed. CLD has a stronger impact on Tmin than on Tmax in winter (Gupta et al., 1993), which explains the high correlation between winter DTR and Tmin. CLD has a warming effect on the nighttime surface temperatures, and hence reducing DTR, due to the fact that clouds emit outgoing longwave radiation back to the surface.

(3) The most striking feature of spring DTR variability is the fact that the first three principal components, which explain together around 42.4% of the total variance, have a strong multidecadal component in the 50-60 years band, which is consistent with those found in the sea level pressure over the northeast Atlantic by Hurrel and Folland (2002). The long-term variation of spring European DTR might be associated with the Atlantic Multidecadal

Oscillation (Delworth and Mann, 2000; Kerr, 2000). Recently, Sutton and Hudson (2005) showed that AMO plays an important role in the modulation of summer climate over Europe. Apparently, AMO plays an important role in other seasons too. For spring, the highest correlations were found with CLD and PET. Although the effect of CLD on DTR has been intensively studied, the effect of PET has not been taken into account. We found that high values of DTR are associated with high values of PET. PET affects mostly Tmax, due to the fact that Tmax is more sensitive to water availability than Tmin (Mitchell et al., 1995). This in agreement with the fact that spring DTR is highly correlated with Tmax than with Tmin (not shown).

(4) During summer, the climate of Europe is mostly influence by blockings. Anomalous barotropic structures are particularly strong (weak) in July (June), when the large scale anomalies are organized in a wavetrain pattern that propagates form the Atlantic Ocean towards Europe (Xoplaki et al., 2003a; Cassou et al., 2005; Corte-Real et al., 1995). High DTR anomalies over the central and eastern part of Europe, in summer, were found to be associated also with a blocking pattern over Europe, characterized by a cyclonic circulation over Scandinavia, anticyclonic circulation over most of Europe and a cyclonic circulation over the Caspian Sea. These kind of blocking situations have a strong impact on the summer extreme temperatures, especially on Tmax, over Europe (Della-Marta et al., 2007; García-Herrera et al., 2010; Feudale and Shukla, 2010). As in the case of spring season, the highest correlations were found between summer PCs and CLD and PET.

(5) The first two leading modes of autumn DTR variability are not associated with the major modes of atmospheric circulation, but they are influenced mostly by wave-train like patterns, which develop over the Atlantic Ocean and extend up to Siberia. The third EOF of autumn DTR variability shows links with the North Atlantic Oscillation. In autumn, the highest correlations were found with CLD and PP. During cold months the water vapor amount is

lower comparing to warm months, which can explain the low correlation with PET in winter and autumn.

(6) The response of DTR to SST was found to be weaker in spring and summer, than for winter and autumn. Cattiaux et al. (2010) found also that the response of land temperatures to SST is season dependent, and this seasonality is due to the warming trends of SST (warming maximum in autumn and a minimum in spring).

(7) The atmospheric pattern associatted to the positive phase of the dominant pattern of DTR variability in winter favors the avection of warm and moist air from the Mediterranean region towards eastern and central Europe, as well as cold air advection towards western Europe. Such a circulation is associatted with positive PP and CLD anomalies over southern and southeastrn Europe and negative anomalies over the northwestern part of Europe. The associted PET pattern shows regional structures which reflect the complexity of the response of PET to atmospheric circulation forcing. The atmospheric circulation patterns associated to the positive phase of the second and third pattern of winter DTR variability are related also with coherent and physicaly consistent patterns of PP and CLD. The corresponding PET pattern shows more regional features.

The DTR patterns from the other seasons are also related with atmospheric circulation through the PP, CLD and PET anomalies. Also in this case, for most of the domain, negative (positive) PP and CLD and positive (negative) PET anomalies lead to positive (negative) DTR anomalies

In conclusion we found that the leading EOF modes of European DTR demonstrate pronounced seasonal differences and their relationship to atmospheric circulation and global SST is also season-dependent. Given the complex nature of this issue, further investigation

and attribution of the spatial dependence of DTR on other climatic parameters (e.g. vapor pressure, soil moisture and wind) are needed.

References

Barnston, A.G., and R.E. Livezey (1987), Classification, seasonality, and persistence of low-frequency atmospheric circulation patterns, *Mon. Wea. Rev., 115,* 1083–1126.

Böhm, R., and I. Auer (1994), A search for greenhouse signal using daytime and nightime temperature series. Heino, R. (ed.), Climate Variations in Europe, Painatuskeskus, Helsinki, pp. 141 – 151.

Braganza, K., D. J. Karoly, and J. M. Arblaster (2004), Diurnal temperature range as an index of global climate change during the twentieth century, *Geophys. Res. Lett., 31*, L13217, doi:10.1029/2004GL019998.

Brázdil, R., R. Machu, and M. Budiková (1994), Temporal and spatial changes in maxima and minima of air temperature in the Czech Republic in the period of 1951–1993, *in* Brázdil, R. and Kolar, M. *(eds.),* Contemporary Climatology, Brno, pp. 93–102.

Briffa, K.R., P.D. Jones, T.S. Bartholin, D. Eckstein, F.H. Schweingruber, W. Karlén, P. Zetterberg, and M. Eronen (1992), Fennoscandian summers from AD 500: temperature changes on short and long timescales, *Clim. Dyn., 7,* 111–119.

Brückner, E. (1890), Klimaschwankungen seit 1700, *Geographische Abhandlungen, 14*, p. 325.

Brunet, M., E. Aguilar, O. Saladié, J. Sigró , and D. López (2001c), The variations and trends of the surface air temperature in the Northeastern Spain from middle nineteenth century onwards, in Detecting and Modelling Regional Climate Change, edited by M. Brunet and D. López, pp. 81– 93, Springer, New York.

Cassou, C., L. Terray, and A. Phillips (2005) Tropical Atlantic influence on European heat waves, *J. Clim. 18*, 2011–2805.

Cattiaux, J., R. Vautard, and P. Yiou (2010), North-Atlantic SST amplified recent wintertime European land temperature extremes and trends, *Clim. Dyn., 36 (11–12),* 2113–2128, doi: 10.1007/s00382-010-0869-0

Compo, G.P., J.S. Whitaker, and P.D. Sardeshmukh (2006), Feasibility of a 100 year reanalysis using only surface pressure data, *Bull. Amer. Met. Soc., 87*, 175-190.

Compo, G.P., J.S. Whitaker, P.D. Sardeshmukh, N. Matsui, R.J. Allan, X. Yin, B.E. Gleason, R.S. Vose, G. Rutledge, P. Bessemoulin, S. Brönnimann, M. Brunet, R.I. Crouthamel,

A.N. Grant, P.Y. Groisman, P.D. Jones, M. Kruk, A.C. Kruger, G.J. Marshall, M. Maugeri, H.Y. Mok, Ø. Nordli, T.F. Ross, R.M. Trigo, X.L. Wang, S.D. Woodruff, and S.J. Worley (2011), The Twentieth Century Reanalysis Project, *Quarterly J. Roy. Meteorol. Soc.*, *137*, 1-28. DOI: 10.1002/qj.776.

Corte-Real, J., X. Zhang, and X. Wang (1995), Large-scale circulation regimes and surface climatic anomalies over the Mediterranean, *Int. J. Climatol.*, *15*, 1135–1150

Dai, A., A.D. DelGenio, and I.Y. Fung (1997), Clouds, precipitation, and temperature range, *Nature*, *386*, 665-666.

Dai, A., K.E. Trenberth, and T.R. Karl, (1999), Effects of clouds, soil moisture, precipitation and water vapor on diurnal temperature range, *J. Clim.*, *12*, 2452-2473.

Dai, A., T. M. L. Wigley, B. A. Boville, J. T. Kiehl, and L. E. Buja (2001), Climates of the 20th and 21st centuries simulated by the NCAR Climate System Model, *J. Clim.*, *14*, 485–519.

Daubechies, I (1990), The wavelet transform, time-frequency localization and signal analysis, *IEEE Trans. Information Theory*, *36*, 965 – 1005.

Della-Marta, P. M., M. R. Haylock, J. Luterbacher, and H. Wanner (2007), Doubled length of western European summer heat waves since 1880, *J. Geophys. Res.*, *112*, D15103.

Delworth, T. L., and M. E. Mann (2000), Observed and simulated multidecadal variability in the Northern Hemisphere, *Clim. Dyn.*, *16*, 661– 676.

Dobesch, H. (1992), On the variations of sunshine duration in Austria, *Theor. App. Climatol*,. *46*, 33-38.

Easterling, D.R., B. Horton, P.D. Jones, T.C. Peterson, T.R. Karl, D.E. Parker, M.J. Salinger, V. Razuvaev, N. Plummer, P. Jamason, and C.K. Folland (1997), Maximum and minimum temperature trends for the globe, *Science*, *277*, 364-367.

Enfield, D.B., A.M. Mestas-Nuñez, and P.J. Trimble (2001), The Atlantic Multidecadal Oscillation and its relation to rainfall and river flows in the continental US, *Geophys. Res. Lett.*, *28*, 2077–2080.

Feudale, L., and J. Shukla (2010), Influence of sea surface temperature on the European heat wave of 2003 summer. Part I: An observational study, *Clim. Dyn.*, *36*, 1691–703.

Fischer, E. M., S. I. Seneviratne, D. Lüthi, and C. Schär (2007a), Contribution of land atmosphere coupling to recent European summer heat waves, *Geophys. Res. Lett.*, *34*, L06707, doi:10.1029/2006GL029068.

Folland, C. K., T. R. Karl, J. R. Christy, R. A. Clarke, G. V. Gruza, J. Jouzel, M. E. Mann, J. Oerlemans, M. J. Salinger, and S.-W. Wang (2001), Observed climate variability and

change. In *Climate change 2001: The scientific basis. Contribution of Working Group I to the Third Assessment Report of the Intergovernmental Panel on Climate Change*, ed. J. T. Houghton, Y. Ding, D. J. Griggs,M. Noguer, P. J. van der Linden, X. Dai, K.Maskell, and C.A. Johnson, 881. Cambridge: Cambridge University Press.

Garcia-Herrera, R., J. Diaz, R.M. Trigo, J. Luterbacher, and E.M. Fischer (2010), A review of the European summer heat wave of 2003, *Critical Reviews in Environmental Science and Technology*, *40***,** 267-306

Gupta, S.K., W. F. Staylor, W. L., Darnell, A. C. Wilber, and N. A. Richey (1993), Seasonal variation of surface and atmospheric cloud radiative forcing over the globe derived from satellite data, *Geophys. Res. Lett.*, *98*, 20761 – 20778.

Henderson – Seller A. (1992), Continental cloudiness changes this century, *Geo J., 27*, 255–76 262. 77

Horton, B. (1995), The geographical distribution of changes in maximum and minimum temperatures, *Atmos. Res.*, *37*, 101–117.

Hoskins, B. J., and T. Ambrizzi (1993), Rossby wave propagation on a realistic longitudinally varying flow, *J. Atmos. Sci., 50***,** 1661–1671.

Hurrell, J. W., and C. K. Folland (2002), A change in the summer atmospheric circulation over the North Atlantic, *CLIVAR Exchanges, 25*, 52-54.

Hurrell, J.W. (1996), Influence of variations in extratropical wintertime teleconnections on Northern Hemisphere temperature, *Geophys. Res. Lett.*, *23*, 665–668.

Jones, P. A. (1991), Historical records of cloud cover and climate for Australia, *Aust. Met. Mag., 39*, 181-189.

Kaas, E., and P. Frich (1995), Diurnal temperature range and cloud cover in the Nordic countries: observed trends and estimates for the future, *Atmos. Res.*, *37*, 211–228.

Karl, T. R., D. Easterling, T. C. Peterson, C. B. Baker, P. D. Jones, G. Kukla, N. Plummer, V. N. Razuvayev, and B. Horton (1994), An update on the asymmetric day/night land surface warming, *in Sixth Conference on Climate Variations, American Meteorological Society*, Nashville, Tennessee, 170–172.

Karl, T. R., P. D. Jones, R.W. Knight, G. Kukla, N. Plummer, V. Razuvayev, K. P. Gallo, J. Lindseay, R. J. Charlson, and T. C. Peterson (1993), Asymmetric trends of daily maximum and minimum temperature, *Bull. Am. Meteorol. Soc.*, *74*, 1007– 1023.

Kerr, R. A. (2000), A North Atlantic climate pacemaker for the centuries, Science, 288, 1984–1985.

Klok, E.J., and A.M.G. Klein Tank (2009), Updated and extended European dataset of daily climate observations, *Int. J. Climatol.*, *29*, 1182, doi:10.1002/joc.1779

Knight, J. R., R. J. Allan, C. K. Folland, M. Vellinga, and M. E. Mann (2005), A signature of persistent natural thermohaline circulation cycles in observed climate. *Geophys. Res. Lett.*, *32***,** L20708, doi:10.1029/2005GL024233

Latif, M., E. Roeckner, M. Botzet, M. Esch, H. Haak, S. Hagemann, J. Jungclaus, S. Legutke, S. Marsland, U. Mikolajewicz, and J. F. B. Mitchell (2004), Reconstructing, monitoring, and predicting multidecadal-scale changes in the North Atlantic thermohaline circulation with sea surface temperature, *J. Climate*, *17***,** 1605–1614.

Makowski, K., M. Wild, and A. Ohmura (2008), Diurnal temperature range over Europe between 1950 and 2005, *Atmos. Chem. Phys.*, *8*, 6483-6498.

Makowski, K., E. B. Jaeger, M. Chiacchio, M. Wild, T. Ewen, and A. Ohmura (2008), On the relationship between diurnal temperature range and surface solar radiation in Europe, JGR - Atmospheres, *J. Geophys. Res.*, *114*, D00D07, doi: 10.1029/2008JD011104.

Makowski, K., and A. Ohmura (2009), Diurnal temperature range, periodic amplitude and surface solar radiation, submitted to *International Journal of Climatology*

Mantua, N.J., S.R. Hare, Y. Zhang, J.M. Wallace, and R.C. Francis (1997), A Pacific decadal climate oscillation with impacts on salmon, *Bull. Amer. Meteor. Soc*, *78*,,1069-1079.

Mesta-Nuñez, A.M., and D.B. Enfield (1999), Rotated global modes of non-ENSO sea surface temperature variability, *J. Climate*, *12*, 2734-2746.

Michaels, P. J., and D. E. Stooksbury (1992), Global warming: A reduced threat?, *Bull. Amer. Meteor. Soc.*, *73/10*, 1563-1577.

Mitchell J. R., Davis W., and C. Senior (1995), On Surface Temperature, Greenhouse Gases, and Aerosols: Models and Observations, *J Clim.*, *8*, 2364 – 2386.

Mitchell T. D., and P. D. Jones (2005), An improved method of constructing a database of monthly climate observations and associated high-resolution grids, *Int. J. Climatology*, *25*, 693-712

Norris, J. R., and M. Wild (2007), Trends in aerosol radiative effects over Europe inferred from observed cloud cover, solar “dimming” and solar “brightening”, *Geophys. Res. Lett.*, *112*, D08214, doi:10.1029/2006JD007794.

Norris, J.R., Y. Zhang, and J.M. Wallace (1998), Role of low clouds in summertime atmosphere-ocean interactions over the North Pacific, *J. Climate, 11*, 2482-2490.

Osborn, T. J., D. Conway, M. Hulme, J. M. Gregory. and P. D. Jones (1999), Air flow influences on local climate: observed and simulated mean relationships for the UK, *Clim. Res., 13*, 173-191.

Philipp, A., P. M. Della-Marta, J. Jacobeit, D. R. Fereday, P. D. Jones, A. Moberg, and H. Wanner (2007), Long-term variability of daily North Atlantic–European pressure patterns since 1850 classified by simulated annealing clustering, *J. Climate, 20***,** 4065–4095

Plantico, M. S., T. R. Karl, G. Kukla, J. Gavin (1990), Is recent climate change across the United States related to rising levels of anthropogenic greenhouse gases?, *J. Geophys. Res., 16*.617-16.637.

Przybylak, R. (2000), Diurnal temperature range in the Arctic and its relation to hemispheric circulation patterns, *Int. J. Climatol, 20***,** 231–253.

Razuvaev, R. N., E. G. Apasova, R. A. Martuganov (1995), Variations in the diurnal temperature range in the European region of the former USSR during the cold season, *Atmos. Res., 37*, 45-51.

Rayner, N. A., D. E. Parker, E. B. Horton, C. K. Folland, L. V. Alexander, D. P. Rowell, E. C. Kent, and A. Kaplan (2003), Globally complete analyses of sea surface temperature, sea ice and night marine air temperature, 1871-2000, *J. Geophy. Res., 108*, 4407, doi:10.1029/2002JD002670.

Saltzman, B., and J. A. Pollack (1977), Sensitivity of the diurnal surface temperature range to changes in physical parameters, *J. Appl. Meteor*., 16, 614–619.

Stone, D. A., and A. J. Weaver (2002), Daily maximum and minimum temperature trends in a climate model, *Geophys. Res. Lett., 29(9)*, 1356, doi:10.1029/2001GL014556.

Stone, D. A., and A. J. Weaver (2003), Factors contributing to diurnal temperature range trends in twentieth and twenty-first century simulations of the CCCma coupled model, *Clim. Dyn., 20*, 435–445.

von Storch, H. and Zwiers, F. W. (1999), Statistical Analysis in Climate Research. Cambridge: Cambridge University Press.

Sutton, R. T., and D. L. R. Hodson (2005), Atlantic Ocean forcing of North American and European summer climate, *Science, 309*, 115–118.

Thompson D. W. J., and J. M. Wallace (1998), The Arctic Oscillation signature in the wintertime geopotential height and temperature fields, *Geophys. Res. Lett., 25*, 1297-1300.

Torrence, C., and G. P. Compo (1998), A practical guide to wavelet analysis. *Bull. Amer. Meteor. Soc., 79*, 61–78.

Trenberth, K. E., P.D. Jones, P. Ambenje, R. Bojariu, D. Easterling, A. Klein Tank, D. Parker, F. Rahimzadeh, J. A. Renwick, M. Rusticucci, B. Soden, P. Zhai (2007), Observations: surface and atmospheric climate change. In: Solomon S, Qin D, Manning M, Marquis M, Averyt K, Tignor MMB, Miller HL Jr, Chen Z (Eds.) Climate Change 2007: The Physical Science Basis. Contribution of Working Group I to the Fourth Assessment Report of the Intergovernmental Panel on Climate Change. Cambridge University Press, Cambridge, 235–336.

Trigo, R.M., T. J. Osborn, and J. M. Corte-Real (2002), The North Atlantic Oscillation influence on Europe: Climate impacts and associated physical mechanisms, *Clim. Res., 20*, 9–17.

Vose, R.S., D.R. Easterling, and B. Gleason (2005a), Maximum and minimum temperature trends for the globe: An update through 2004, *Geophys. Res. Lett., 32*, L23822, doi:10.1029/2004GL024379.

Wallace, J. M., and D. S. Gutzler (1981), Teleconnections in the geopotential height field during the Northern Hemisphere winter, *Mon. Wea. Rev., 109*, 784–812.

Wang, N., L.G.. Thompson, and J. Cole-Dai (2000) The nature of the solar activity during the Maunder Minimum revealed by the Guliya ice core record, *Chinese Sci. Bull., 45* (23), 2118–2124.

Weber, G. R. (1990a), Spatial and temporal variations of sunshine in the Federal Republic of Germany, *Theor. Appl. Climatol., 41*, 1-9.

Whitaker, J.S., G.P.Compo, X. Wei, and T.M. Hamill (2004), Reanalysis without radiosondes using ensemble data assimilation, *Mon. Wea. Rev., 132*, 1190-1200.

Xoplaki, E., J. F. Gonzalez-Rouco, J. Luterbacher, H. Wanner (2003a), Mediterranean summer air temperature variability and its connection to the large-scale atmospheric circulation and SSTs, *Clim. Dyn., 20*, 723–739 DOI 10.1007/s00382-003-0304-x

Zhou, L., R. E. Dickinson, Y. Tian, R. Vose, and Y. Dai (2007), Impact of vegetation removal and soil aridation on diurnal temperature range in a semiarid region: Application to the Sahel, *Proc. Natl. Acad. Sci. U. S. A., 104*, 17.937– 17.942.

Zveryaev I. I., and S. K. Gulev (2009), Seasonality in secular changes and interannual variability of European air temperature during the twentieth century, *J. Geophys. Res.*, *114*, D02110, doi:10.1029/2008JD010624.

Table 1. Teleconnection indices used in this study, time period and their source

Name	**Explanation**	**Period**	**Data source**
AMO	Atlantic Multidecadal Oscilation	1901-2008	http://climexp.knmi.nl/data/iamo_hadsst2.dat
NAO	North Atlantic Oscillation	1901-2008	http://www.cru.uea.ac.uk/cru/data/nao.htm
AO	Arctic Oscillation	1901-2008	http://www.atmos.colostate.edu/ao/Data/ao_index.html
SCA	Scandinavian Pattern	1950-2001	http://www.cpc.noaa.gov/data/teledoc/scand.shtml

Table 2. The years corresponding to the ***Low*** values of the seasonal PCs (< - 1 std. dev.) and ***High*** values of the seasonal PCs (> 1 std. dev.) used for the composite map analysis in Section 3.

DJF						**MAM**						**JJA**						**SON**					
PC1		**PC2**		**PC3**		**PC1**		**PC2**		**PC3**		**PC1**		**PC2**		**PC3**		**PC1**		**PC2**		**PC3**	
Low	*High*	Low	*High*	Low	*High*	Low	*High*	Low	*High*	Low	*High*	Low	*High*	Low	*High*	Low	*High*	Low	*High*	Low	*High*	Low	*High*
1902	*1910*	1904	*1903*	1927	*1904*	1909	*1915*	1908	*1934*	1901	*1907*	1901	*1923*	1901	*1908*	1902	*1910*	1901	*1905*	1927	*1906*	1904	*1917*
1940	*1915*	1919	*1932*	1928	*1906*	1912	*1918*	1940	*1935*	1903	*1909*	1939	*1928*	1934	*1909*	1904	*1920*	1907	*1912*	1932	*1908*	1909	*1929*
1942	*1923*	1923	*1940*	1930	*1909*	1924	*1921*	1941	*1938*	1920	*1912*	1947	*1931*	1935	*1910*	1906	*1924*	1919	*1931*	1934	*1911*	1910	*1935*
1956	*1925*	1931	*1943*	1934	*1910*	1926	*1934*	1942	*1943*	1930	*1933*	1955	*1954*	1938	*1912*	1911	*1927*	1920	*1935*	1935	*1912*	1960	*1947*
1963	*1930*	1935	*1949*	1935	*1913*	1927	*1940*	1956	*1945*	1934	*1938*	1959	*1962*	1939	*1913*	1921	*1931*	1921	*1936*	1938	*1914*	1968	*1948*
1964	*1931*	1969	*1950*	1936	*1914*	1944	*1942*	1958	*1947*	1936	*1941*	1968	*1978*	1943	*1914*	1935	*1936*	1942	*1940*	1942	*1916*	1974	*1953*
1968	*1933*	1970	*1952*	1937	*1915*	1967	*1943*	1960	*1949*	1963	*1942*	1969	*1981*	1946	*1916*	1947	*1938*	1947	*1950*	1943	*1920*	1975	*1954*
1970	*1936*	1972	*1956*	1939	*1916*	1970	*1946*	1963	*1950*	1972	*1943*	1970	*1985*	1947	*1925*	1949	*1939*	1949	*1952*	1944	*1921*	1976	*1957*
1976	*1937*	1973	*1957*	1942	*1918*	1977	*1947*	1964	*1961*	1975	*1944*	1972	*1987*	1950	*1926*	1950	*1948*	1951	*1960*	1949	*1922*	1980	*1959*
1979	*1939*	1978	*1958*	1943	*1920*	1978	*1948*	1965	*1968*	1979	*1945*	1973	*1990*	1951	*1955*	1952	*1954*	1955	*1974*	1957	*1941*	1988	*1962*
1982	*1944*	1979	*1959*	1945	*1922*	1979	*1949*	1969	*1986*	1983	*1948*	1975	*1993*	1952	*1958*	1976	*1956*	1965	*1981*	1963	*1947*	1992	*1969*
1985	*1945*	1986	*1975*	1946	*1963*	1982	*1952*	1978	*1989*	1985	*1953*	1992	*1998*	1957	*1969*	1983	*1960*	1969	*1984*	1966	*1959*	1993	*1970*
1986	*1952*	1988	*1989*	1947	*1966*	1983	*1953*	1980	*1990*	1986	*1954*	1997	*2000*	1961	*1976*	1989	*1966*	1971	*1987*	1967	*1971*	1994	*1986*
1987	*1957*	1996	*1990*	1950	*1981*	1991	*1956*	1981	*1995*	1999	*1955*	1999		1963	*1977*	1990	*1972*	1973	*1998*	1974	*1973*	1995	*1989*
2003	*1961*	2003	*1995*	1951	*1982*	1992	*1957*	1984	*1997*		*1956*	2002		1964	*1980*	1994	*1979*	1975		1975	*1985*	1998	*2006*
	1973	2009	*2000*	1954	*1983*	1994	*1960*	1988	*2000*		*1961*	2006		2007	*1982*	2003	*1980*	1983		1984	*1996*	2001	
	1995			1956	*1997*	1995	*1963*	1996	*2003*		*1974*			2008	*1988*	2006	*1981*	1988		1994	*2003*		
	2001			1964	*2000*		*1968*	1998	*2007*		*1976*				*1997*		*2002*	1995		1998			
	2005			1967	*2003*		*1969*	2006			*1982*							2005					
	2008			1969	*2004*		*1990*				*1997*												
				1972			*2002*				*2004*												
				1973			*2003*																
							2007																
15	***20***	**16**	***16***	**22**	***20***	**17**	***23***	**19**	***18***	**14**	***21***	**16**	***13***	**17**	***18***	**17**	***18***	**19**	***14***	**18**	***17***	**16**	***15***

Figure 1.

a) Spatial patterns of the first winter EOF mode of the DTR field;

b) Spatial patterns of the second winter EOF mode of the DTR field;

c) Spatial patterns of the third winter EOF mode of the DTR field;

d) The times series of the first Principal Component (PC1) corresponding to the first winter EOF mode (black line); its corresponding 7-yr running mean (red line) and the winter NAO index (magenta bars)

(The NAO index (magenta bars) is multiplied with (-1) for a better comparison to winter PC1);

e) The times series of the second Principal Component (PC2) corresponding to the second winter EOF mode (blue line); its corresponding 7-yr running mean (red line) and the winter SCA index (orange line) (The SCA index (orange bars) is multiplied with (-1) for a better comparison to winter PC2);

f) The times series of the third Principal Component (PC3) corresponding to the third winter EOF mode (green line); its corresponding 7-yr running means (red line) and the 7-yr running mean of the winter AMO index (blue line);

g) The continuous wavelet power spectrum of winter PC1 (The thick black contour is the 5% significance level against red noise);

h) The continuous wavelet power spectrum of winter PC2;

i) The continuous wavelet power spectrum of winter PC3;

Figure 2.

a) Spatial patterns of the first spring EOF mode of the DTR field;

b) Spatial patterns of the second spring EOF mode of the DTR field;

c) Spatial patterns of the third spring EOF mode of the DTR field;

d) The times series of the first Principal Component (PC1) corresponding to the first spring EOF mode (black line) and its corresponding 7-yr running mean (red line);

e) The times series of the second Principal Component (PC2) corresponding to the second spring EOF mode (blue line); its corresponding 7-yr running mean (red line) and the spring AO index (orange line);

f) The times series of the third Principal Component (PC3) corresponding to the third spring EOF mode (green line) and its corresponding 7-yr running means (red line);

g) The continuous wavelet power spectrum of spring PC1 (The thick black contour is the 5% significance level against red noise);

h) The continuous wavelet power spectrum of spring PC2;

i) The continuous wavelet power spectrum of spring PC3;

Figure 3.

a) Spatial patterns of the first summer EOF mode of the DTR field;

b) Spatial patterns of the second summer EOF mode of the DTR field;

c) Spatial patterns of the third summer EOF mode of the DTR field;

d) The times series of the first Principal Component (PC1) corresponding to the first summer EOF mode (black line); its corresponding 7-yr running mean (red line) and the summer SCA index (magenta bars);

e) The times series of the second Principal Component (PC2) corresponding to the second summer EOF mode (blue line) and its corresponding 7-yr running mean (red line);

f) The times series of the third Principal Component (PC3) corresponding to the third summer EOF mode (green line) and its corresponding 7-yr running means (red line);

g) The continuous wavelet power spectrum of summer PC1 (The thick black contour is the 5% significance level against red noise);

h) The continuous wavelet power spectrum of summer PC2;

i) The continuous wavelet power spectrum of summer PC3;

Figure 4.

a) Spatial patterns of the first autumn EOF mode of the DTR field;

b) Spatial patterns of the second autumn EOF mode of the DTR field;

c) Spatial patterns of the third autumn EOF mode of the DTR field;

d) The times series of the first Principal Component (PC1) corresponding to the first autumn EOF mode (black line) and its corresponding 7-yr running mean (red line);

e) The times series of the second Principal Component (PC2) corresponding to the second autumn EOF mode (blue line) and its corresponding 7-yr running mean (red line;

f) The times series of the third Principal Component (PC3) corresponding to the third autumn EOF mode (green line), its corresponding 7-yr running means (red line) and the autumn NAO index (blue line);

g) The continuous wavelet power spectrum of autumn PC1 (The thick black contour is the 5% significance level against red noise);

h) The continuous wavelet power spectrum of autumn PC2;

i) The continuous wavelet power spectrum of autumn PC3;

Figure 5.

a) The difference (high – low) between the composite maps of winter Z500 for the years when winter PC1 was high (std. dev.> 1) and low (std. dev.< -1) , respectively;

b) As in Figure 5a, but for winter PC2;

c) As in Figure 5a, but for winter PC3;

d) The difference (high – low) between the composite maps of winter SST for the years when winter PC1 was high (std. dev.> 1) and low (std. dev.< -1) , respectively;

e) As in Figure 5d, but for winter PC2;

f) As in Figure 5d, but for winter PC3;

(The black contour lines indicate the Z500 and SST normalized anomalies significant at 95 % significance level on a standard t-test).

Figure 6.

a) The difference (high – low) between the composite maps of spring Z500 for the years when spring PC1 was high (std. dev.> 1) and low (std. dev.< -1) , respectively;

b) As in Figure 6a, but for spring PC2;

c) As in Figure 6a, but for spring PC3;

d) The difference (high – low) between the composite maps of spring SST for the years when spring PC1 was high (std. dev.> 1) and low (std. dev.< -1) , respectively;

e) As in Figure 6d, but for spring PC2;

f) As in Figure 6d, but for spring PC3;

(The black contour lines indicate the Z500 and SST normalized anomalies significant at 95 % significance level on a standard t-test).

Figure 7.

a) The difference (high – low) between the composite maps of summer Z500 for the years when summer PC1 was high (std. dev.> 1) and low (std. dev.< -1) , respectively;

b) As in Figure 7a, but for summer PC2;

c) As in Figure 7a, but for summer PC3;

d) The difference (high – low) between the composite maps of summer SST for the years when summer PC1 was high (std. dev.> 1) and low (std. dev.< -1) , respectively;

e) As in Figure 7d, but for summer PC2;

f) As in Figure 7d, but for summer PC3;

(The black contour lines indicate the Z500 and SST normalized anomalies significant at 95 % significance level on a standard t-test).

Figure 8.

a) The difference (high – low) between the composite maps of autumn Z500 for the years when autumn PC1 was high (std. dev.> 1) and low (std. dev.< -1) , respectively;

b) As in Figure 8a, but for autumn PC2;

c) As in Figure 8a, but for autumn PC3;

d) The difference (high – low) between the composite maps of autumn SST for the years when autumn PC1 was high (std. dev.> 1) and low (std. dev.< -1) , respectively;

e) As in Figure 8d, but for autumn PC2;

f) As in Figure 8d, but for autumn PC3;

(The black contour lines indicate the Z500 and SST normalized anomalies significant at 95 % significance level on a standard t-test).

Figure 9.

a) The correlation maps between winter PC1 and winter precipitation (PP);

b) The correlation maps between winter PC2 and winter precipitation (PP);

c) The correlation maps between winter PC3 and winter precipitation(PP);

d) The correlation maps between winter PC1 and winter cloud cover (CLD);

e) The correlation maps between winter PC2 and winter cloud cover (CLD);

f) The correlation maps between winter PC3 and winter cloud cover (CLD);

g) The correlation maps between winter PC1 and winter potential evapotranspiration (PET);

h) The correlation maps between winter PC2 and winter potential evapotranspiration (PET);

i) The correlation maps between winter PC3 and winter potential evapotranspiration (PET).

Figure 10.

a) The correlation maps between spring PC1 and spring precipitation (PP);

b) The correlation maps between spring PC2 and spring precipitation (PP);

c) The correlation maps between spring PC3 and spring precipitation(PP);

d) The correlation maps between spring PC1 and spring cloud cover (CLD);

e) The correlation maps between spring PC2 and spring cloud cover (CLD);

f) The correlation maps between spring PC3 and spring cloud cover (CLD);

g) The correlation maps between spring PC1 and spring potential evapotranspiration (PET);

h) The correlation maps between spring PC2 and spring potential evapotranspiration (PET);

i) The correlation maps between spring PC3 and spring potential evapotranspiration (PET).

Figure 11.

a) The correlation maps between summer PC1 and summer precipitation (PP);

b) The correlation maps between summer PC2 and summer precipitation (PP);

c) The correlation maps between summer PC3 and summer precipitation(PP);

d) The correlation maps between summer PC1 and summer cloud cover (CLD);

e) The correlation maps between summer PC2 and summer cloud cover (CLD);

f) The correlation maps between summer PC3 and summer cloud cover (CLD);

g) The correlation maps between summer PC1 and summer potential evapotranspiration (PET);

h) The correlation maps between summer PC2 and summer potential evapotranspiration (PET);

i) The correlation maps between summer PC3 and summer potential evapotranspiration (PET).

Figure 12.

a) The correlation maps between autumn PC1 and autumn precipitation (PP);

b) The correlation maps between autumn PC2 and autumn precipitation (PP);

c) The correlation maps between autumn PC3 and autumn precipitation(PP);

d) The correlation maps between autumn PC1 and autumn cloud cover (CLD);

e) The correlation maps between autumn PC2 and autumn cloud cover (CLD);

f) The correlation maps between autumn PC3 and autumn cloud cover (CLD);

g) The correlation maps between autumn PC1 and autumn potential evapotranspiration (PET);

h) The correlation maps between autumn PC2 and autumn potential evapotranspiration (PET);

i) The correlation maps between autumn PC3 and autumn potential evapotranspiration (PET).

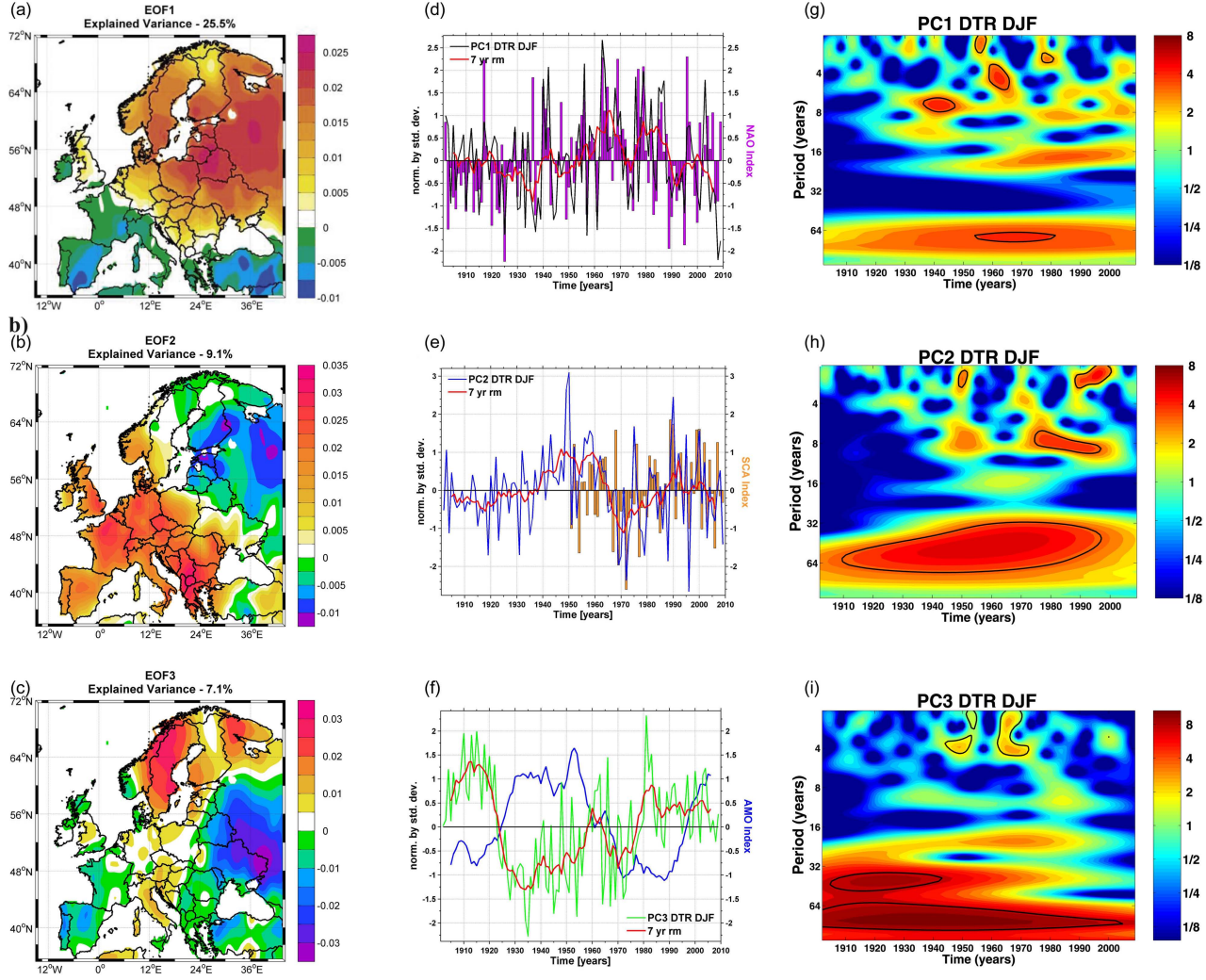
(a)
EOF1
Explained Variance - 25.5%
(b)
EOF2
Explained Variance - 9.1%
(c)
EOF3
Explained Variance - 7.1%
(d)
PC1 DTR DJF
7 yr rm
NAO Index
(e)
PC2 DTR DJF
7 yr rm
SCA Index
(f)
PC3 DTR DJF
7 yr rm
AMO Index
norm. by std. dev.
Time [years]
(g)
PC1 DTR DJF
(h)
PC2 DTR DJF
(i)
PC3 DTR DJF
Period (years)
Time (years)

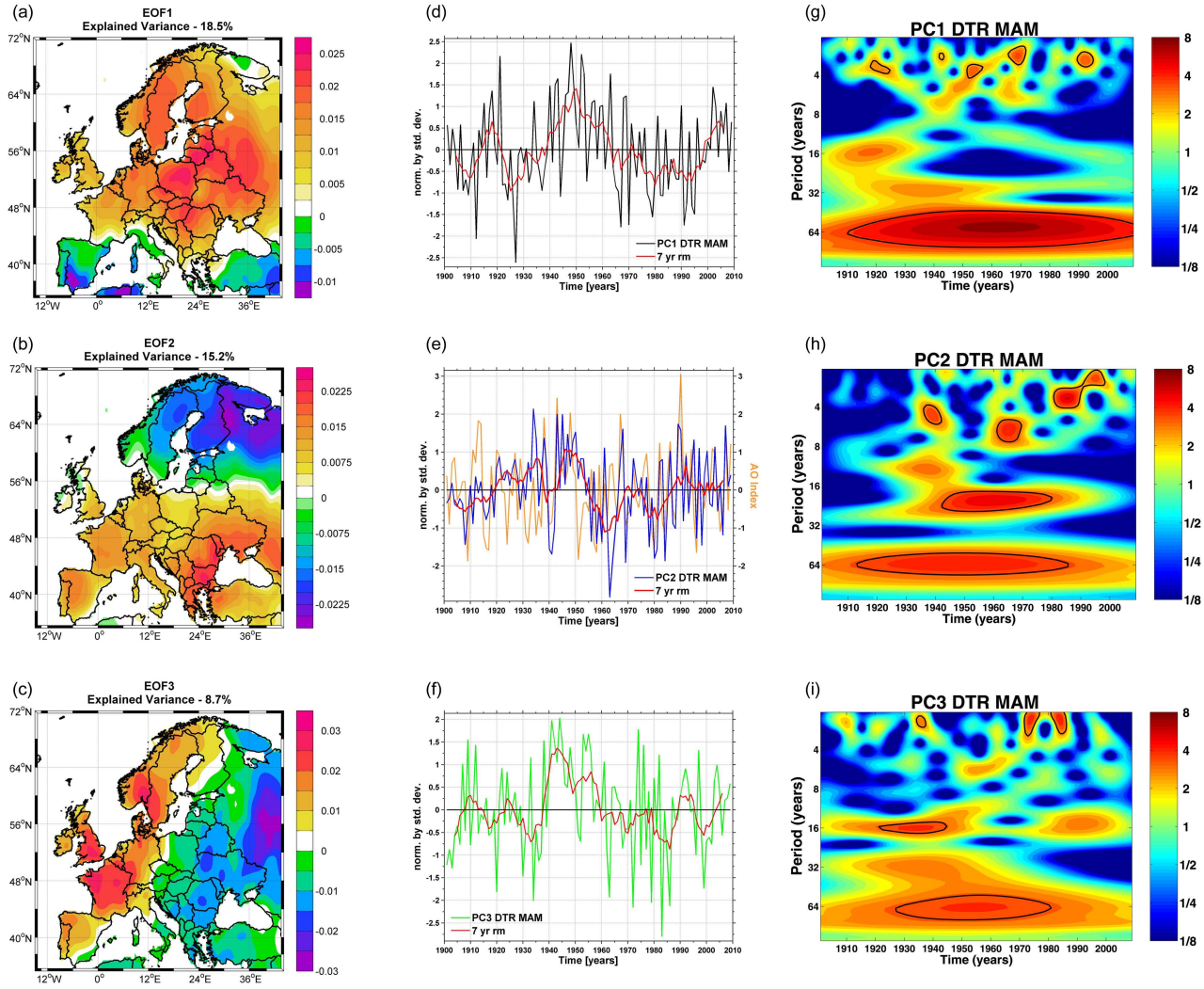
(a)
EOF1
Explained Variance - 18.5%
(b)
EOF2
Explained Variance - 15.2%
(c)
EOF3
Explained Variance - 8.7%
72°N
64°N
56°N
48°N
40°N
12°W
0°
12°E
24°E
36°E
(d)
(e)
(f)
norm. by std. dev.
PC1 DTR MAM
PC2 DTR MAM
PC3 DTR MAM
7 yr rm
AO Index
Time [years]
(g)
(h)
(i)
PC1 DTR MAM
PC2 DTR MAM
PC3 DTR MAM
Period (years)
Time (years)

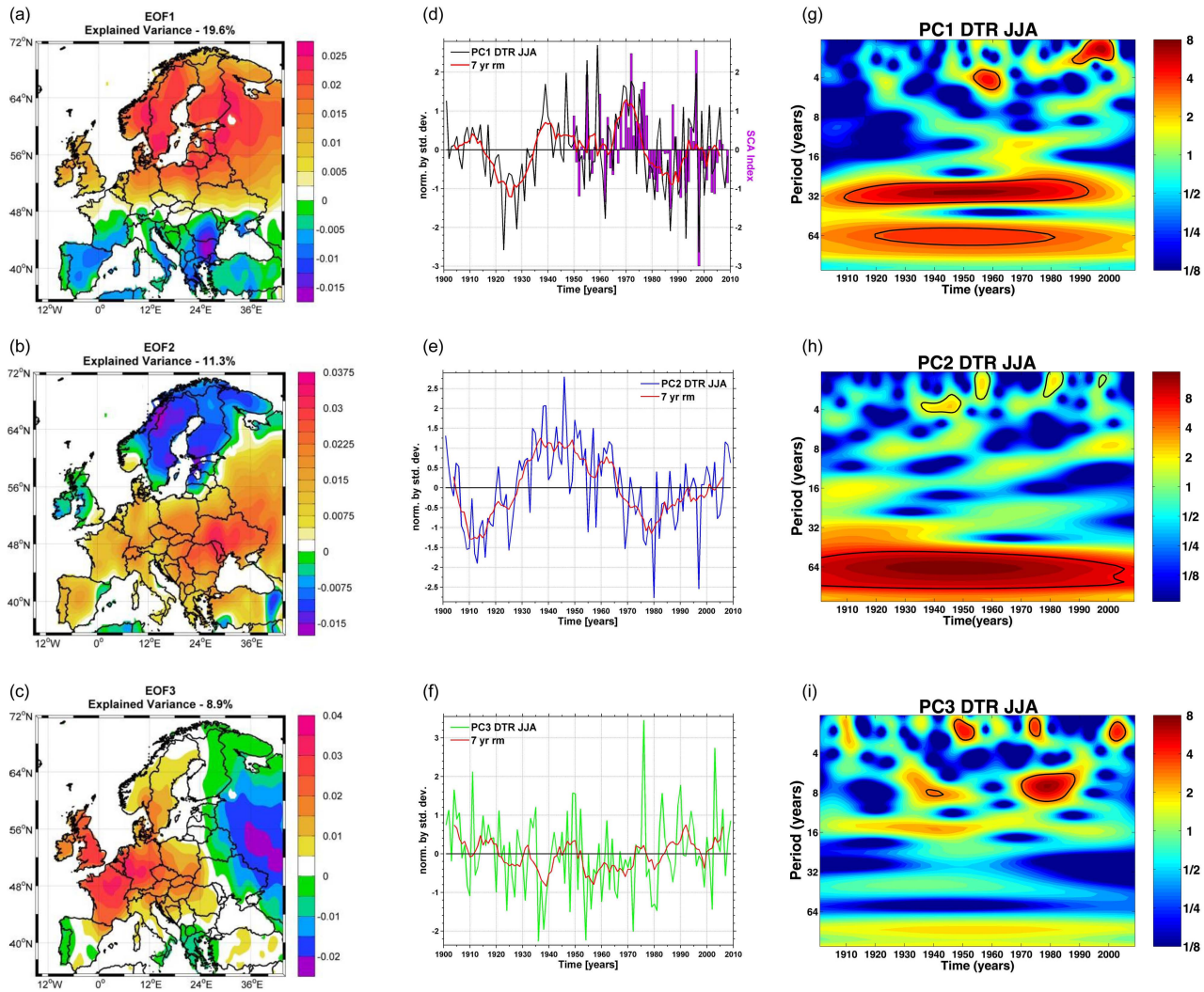
(a)
EOF1
Explained Variance - 19.6%
(b)
EOF2
Explained Variance - 11.3%
(c)
EOF3
Explained Variance - 8.9%
(d)
PC1 DTR JJA
7 yr rm
norm. by std. dev.
SOA Index
Time [years]
(e)
PC2 DTR JJA
7 yr rm
norm. by std. dev.
Time [years]
(f)
PC3 DTR JJA
7 yr rm
norm. by std. dev.
Time [years]
(g)
PC1 DTR JJA
Period (years)
Time (years)
(h)
PC2 DTR JJA
Period (years)
Time(years)
(i)
PC3 DTR JJA
Period (years)
Time (years)

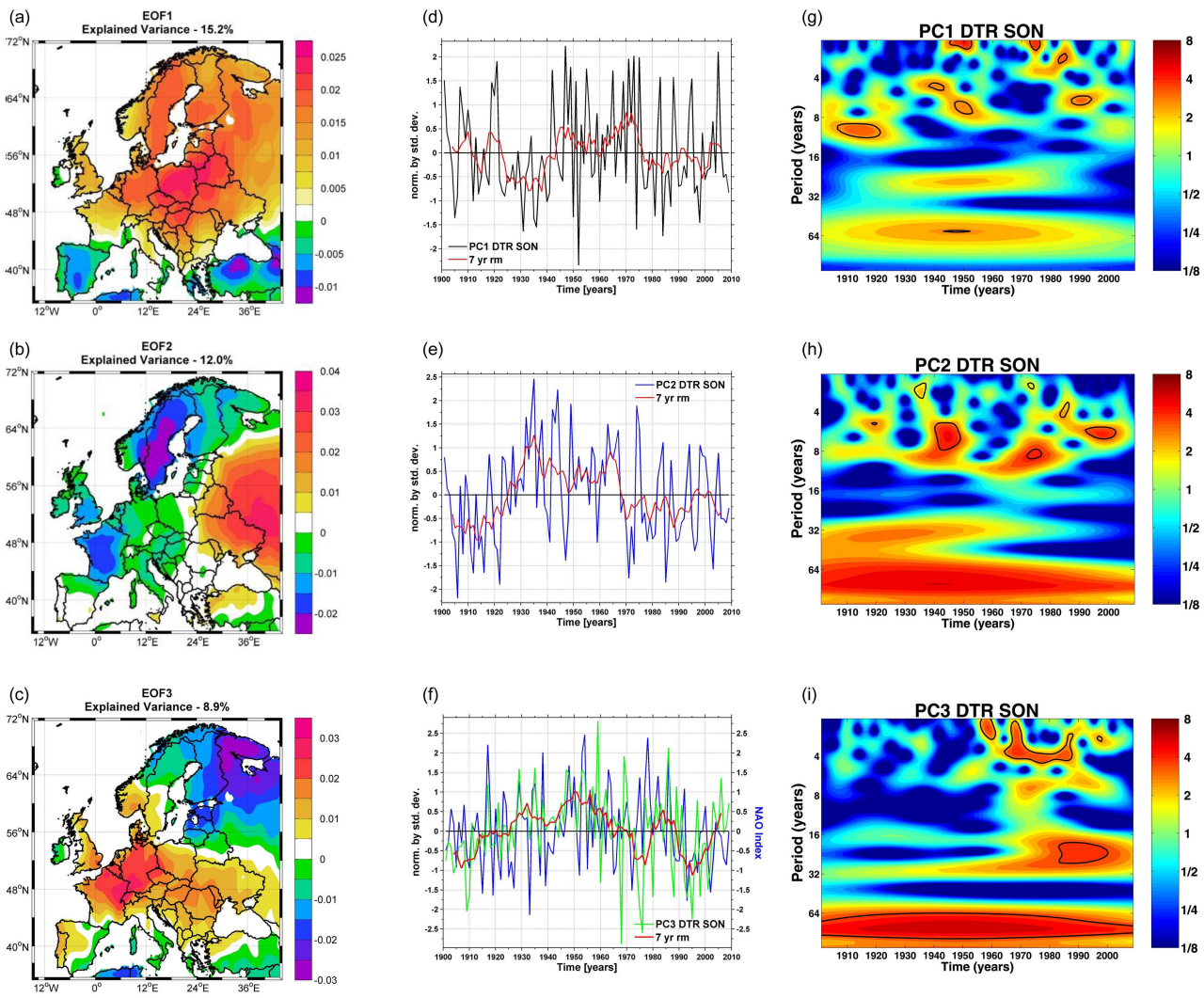
(a)
EOF1
Explained Variance - 15.2%
72°N
64°N
56°N
48°N
40°N
12°W
0°
12°E
24°E
36°E
0.025
0.02
0.015
0.01
0.005
0
-0.005
-0.01
(b)
EOF2
Explained Variance - 12.0%
0.04
0.03
0.02
0.01
0
-0.01
-0.02
(c)
EOF3
Explained Variance - 8.9%
0.03
0.02
0.01
0
-0.01
-0.02
-0.03
(d)
norm. by std. dev.
PC1 DTR SON
7 yr rm
Time [years]
(e)
PC2 DTR SON
7 yr rm
(f)
PC3 DTR SON
7 yr rm
NAO Index
(g)
PC1 DTR SON
Period (years)
Time (years)
(h)
PC2 DTR SON
(i)
PC3 DTR SON

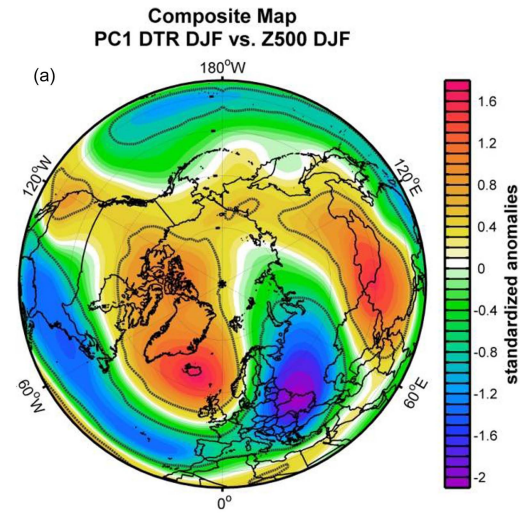
Composite Map
PC1 DTR DJF vs. Z500 DJF
(a)
180°W
120°W
120°E
60°W
60°E
0°
1.6
1.2
0.8
0.4
0
-0.4
-0.8
-1.2
-1.6
-2
standardized anomalies

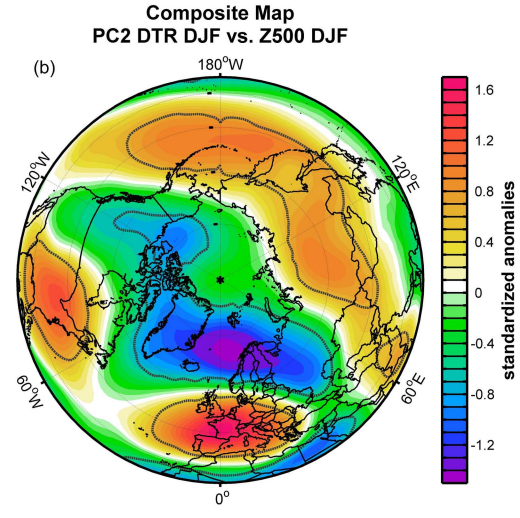
Composite Map
PC2 DTR DJF vs. Z500 DJF
(b)
180°W
120°W
120°E
60°W
60°E
0°
1.6
1.2
0.8
0.4
0
-0.4
-0.8
-1.2
standardized anomalies

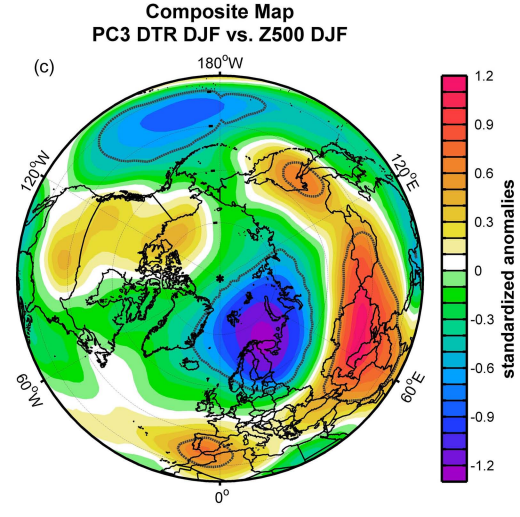
Composite Map
PC3 DTR DJF vs. Z500 DJF
(c)
180°W
120°W
120°E
60°W
60°E
0°
1.2
0.9
0.6
0.3
0
-0.3
-0.6
-0.9
-1.2
standardized anomalies

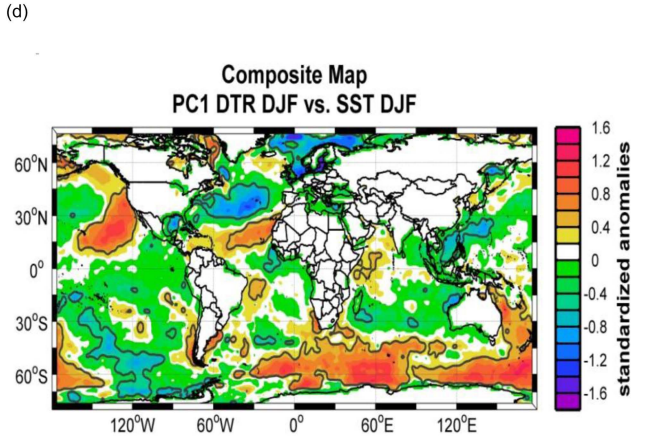
(d)
Composite Map
PC1 DTR DJF vs. SST DJF
60°N
30°N
0°
30°S
60°S
120°W
60°W
0°
60°E
120°E
1.6
1.2
0.8
0.4
0
-0.4
-0.8
-1.2
-1.6
standardized anomalies

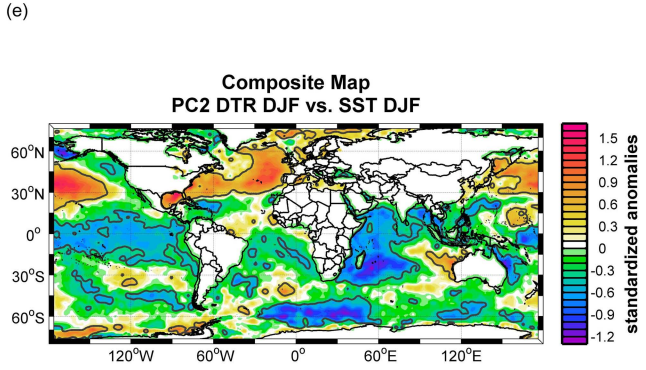
(e)
Composite Map
PC2 DTR DJF vs. SST DJF
60°N
30°N
0°
30°S
60°S
120°W
60°W
0°
60°E
120°E
1.5
1.2
0.9
0.6
0.3
0
-0.3
-0.6
-0.9
-1.2
standardized anomalies

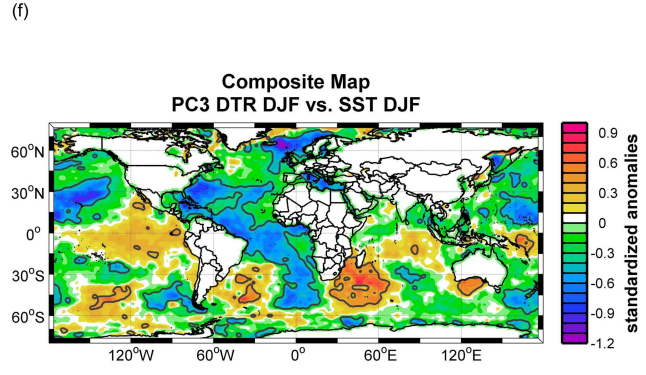
(f)
Composite Map
PC3 DTR DJF vs. SST DJF
60°N
30°N
0°
30°S
60°S
120°W
60°W
0°
60°E
120°E
0.9
0.6
0.3
0
-0.3
-0.6
-0.9
-1.2
standardized anomalies

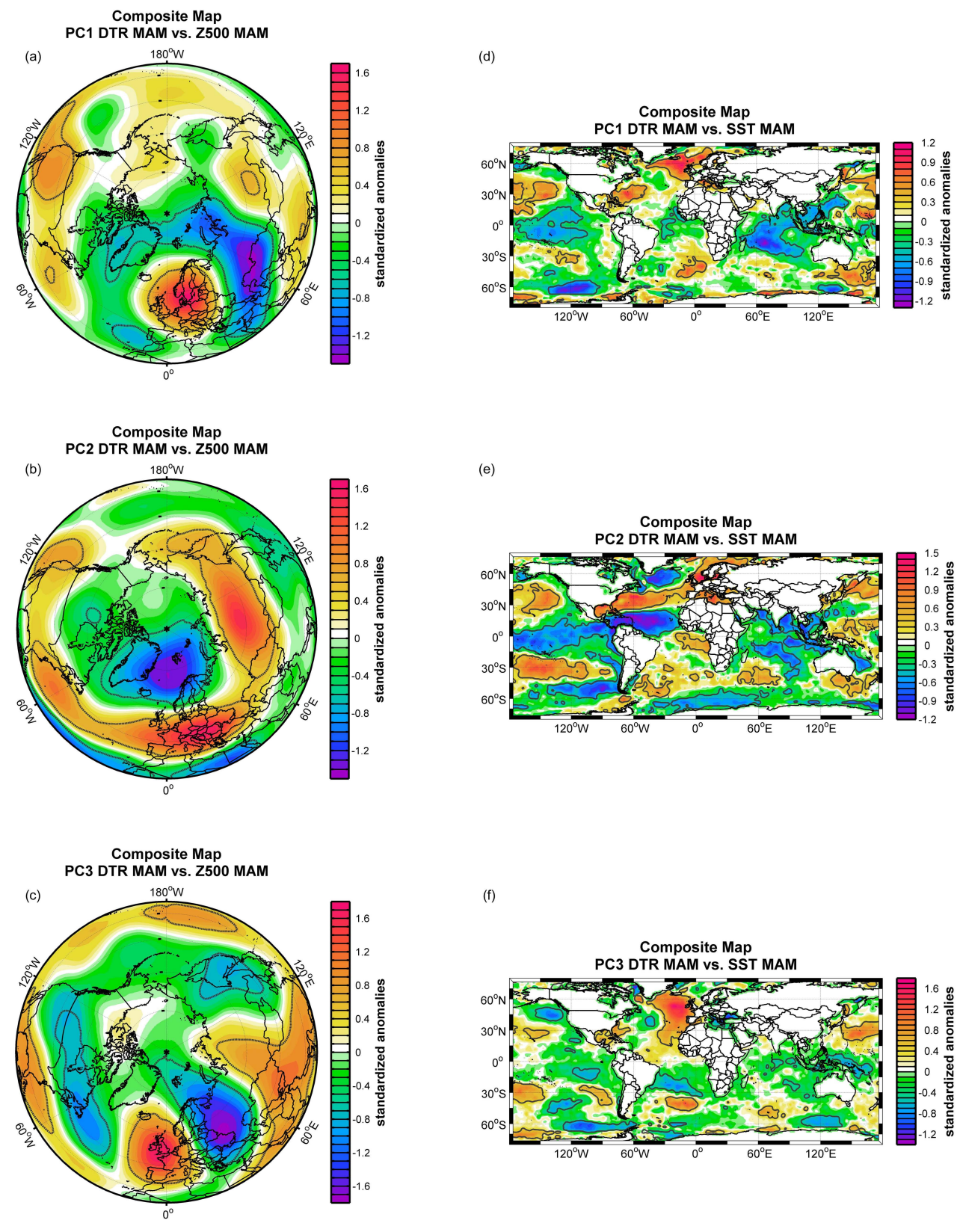
Composite Map
PC1 DTR MAM vs. Z500 MAM
(a)
180°W
120°W
120°E
60°W
60°E
0°
standardized anomalies
1.6
1.2
0.8
0.4
0
-0.4
-0.8
-1.2
Composite Map
PC2 DTR MAM vs. Z500 MAM
(b)
Composite Map
PC3 DTR MAM vs. Z500 MAM
(c)
(d)
Composite Map
PC1 DTR MAM vs. SST MAM
60°N
30°N
0°
30°S
60°S
120°W
60°W
0°
60°E
120°E
1.2
0.9
0.6
0.3
0
-0.3
-0.6
-0.9
-1.2
(e)
Composite Map
PC2 DTR MAM vs. SST MAM
1.5
(f)
Composite Map
PC3 DTR MAM vs. SST MAM

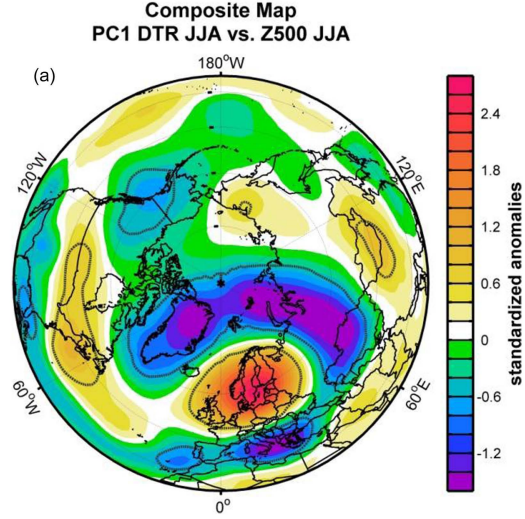
Composite Map
PC1 DTR JJA vs. Z500 JJA
(a)
180°W
120°W
120°E
60°W
60°E
0°
2.4
1.8
1.2
0.6
0
-0.6
-1.2
standardized anomalies

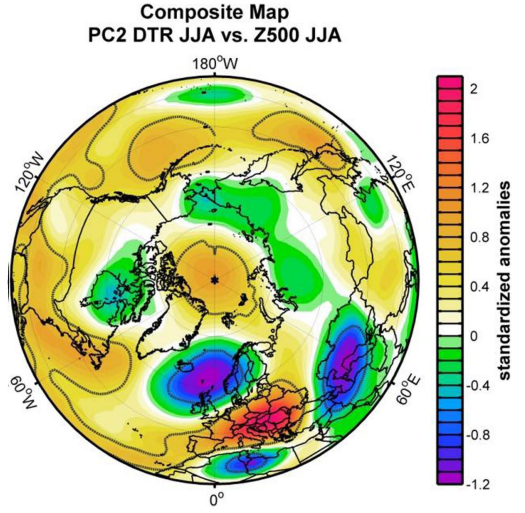
Composite Map
PC2 DTR JJA vs. Z500 JJA
180°W
120°W
120°E
60°W
60°E
0°
2
1.6
1.2
0.8
0.4
0
-0.4
-0.8
-1.2
standardized anomalies

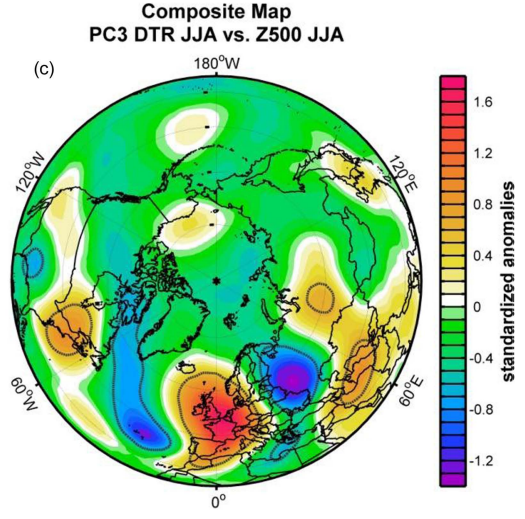
Composite Map
PC3 DTR JJA vs. Z500 JJA
(c)
180°W
120°W
120°E
60°W
60°E
0°
1.6
1.2
0.8
0.4
0
-0.4
-0.8
-1.2
standardized anomalies

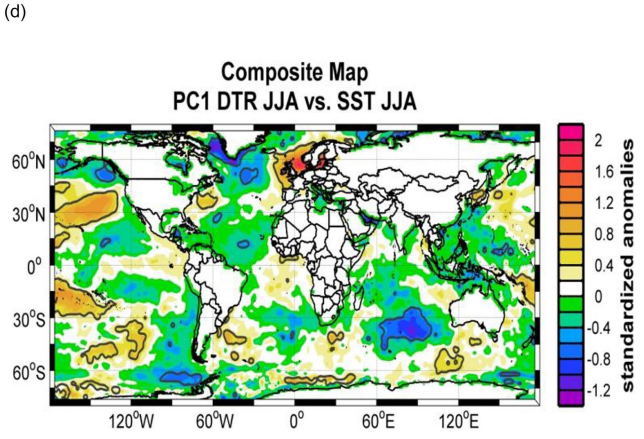
(d)
Composite Map
PC1 DTR JJA vs. SST JJA
60°N
30°N
0°
30°S
60°S
120°W
60°W
0°
60°E
120°E
2
1.6
1.2
0.8
0.4
0
-0.4
-0.8
-1.2
standardized anomalies

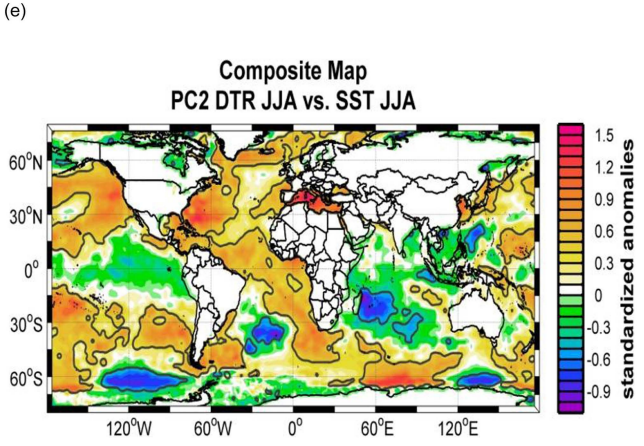
(e)
Composite Map
PC2 DTR JJA vs. SST JJA
60°N
30°N
0°
30°S
60°S
120°W
60°W
0°
60°E
120°E
1.5
1.2
0.9
0.6
0.3
0
-0.3
-0.6
-0.9
standardized anomalies

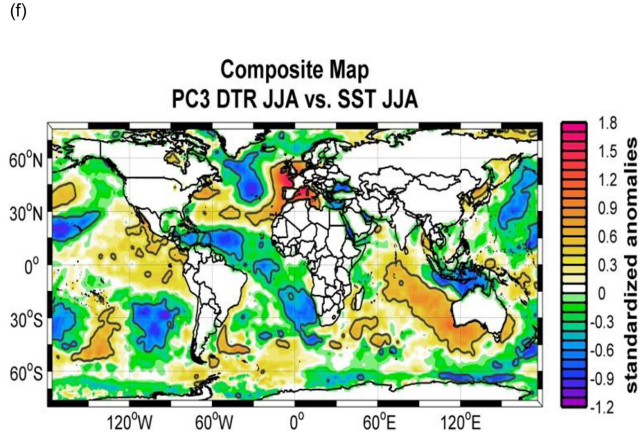
(f)
Composite Map
PC3 DTR JJA vs. SST JJA
60°N
30°N
0°
30°S
60°S
120°W
60°W
0°
60°E
120°E
1.8
1.5
1.2
0.9
0.6
0.3
0
-0.3
-0.6
-0.9
-1.2
standardized anomalies

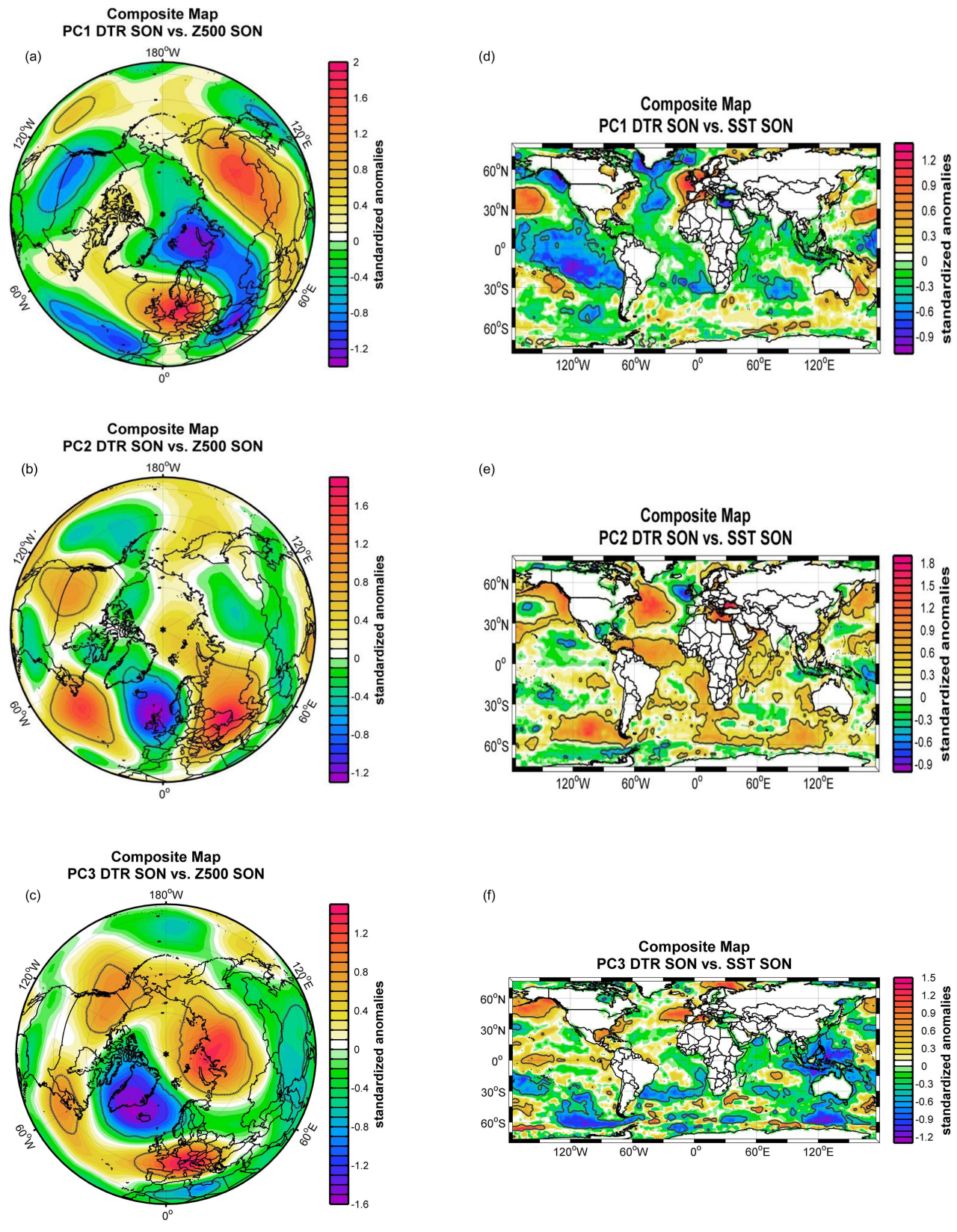
(a)
Composite Map
PC1 DTR SON vs. Z500 SON
180°W
120°W
120°E
60°W
60°E
0°
standardized anomalies
2
1.6
1.2
0.8
0.4
0
-0.4
-0.8
-1.2
(b)
Composite Map
PC2 DTR SON vs. Z500 SON
180°W
120°W
120°E
60°W
60°E
0°
standardized anomalies
1.6
1.2
0.8
0.4
0
-0.4
-0.8
-1.2
(c)
Composite Map
PC3 DTR SON vs. Z500 SON
180°W
120°W
120°E
60°W
60°E
0°
standardized anomalies
1.2
0.8
0.4
0
-0.4
-0.8
-1.2
-1.6
(d)
Composite Map
PC1 DTR SON vs. SST SON
60°N
30°N
0°
30°S
60°S
120°W
60°W
0°
60°E
120°E
standardized anomalies
1.2
0.9
0.6
0.3
0
-0.3
-0.6
-0.9
(e)
Composite Map
PC2 DTR SON vs. SST SON
60°N
30°N
0°
30°S
60°S
120°W
60°W
0°
60°E
120°E
standardized anomalies
1.8
1.5
1.2
0.9
0.6
0.3
0
-0.3
-0.6
-0.9
(f)
Composite Map
PC3 DTR SON vs. SST SON
60°N
30°N
0°
30°S
60°S
120°W
60°W
0°
60°E
120°E
standardized anomalies
1.5
1.2
0.9
0.6
0.3
0
-0.3
-0.6
-0.9
-1.2

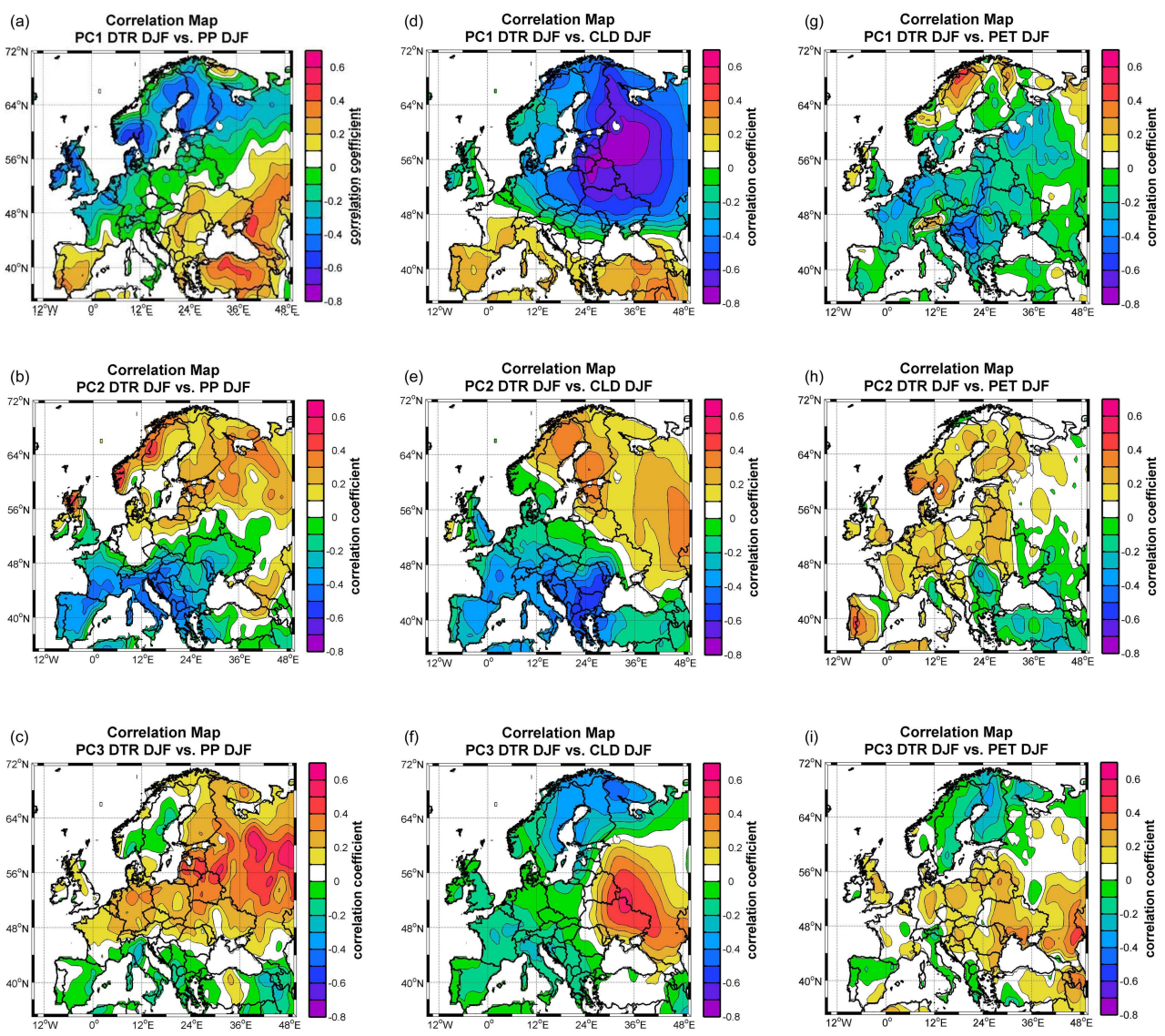
(a)
Correlation Map
PC1 DTR DJF vs. PP DJF
(b)
Correlation Map
PC2 DTR DJF vs. PP DJF
(c)
Correlation Map
PC3 DTR DJF vs. PP DJF
(d)
Correlation Map
PC1 DTR DJF vs. CLD DJF
(e)
Correlation Map
PC2 DTR DJF vs. CLD DJF
(f)
Correlation Map
PC3 DTR DJF vs. CLD DJF
(g)
Correlation Map
PC1 DTR DJF vs. PET DJF
(h)
Correlation Map
PC2 DTR DJF vs. PET DJF
(i)
Correlation Map
PC3 DTR DJF vs. PET DJF
72°N
64°N
56°N
48°N
40°N
12°W
0°
12°E
24°E
36°E
48°E
correlation coefficient
0.6
0.4
0.2
0
-0.2
-0.4
-0.6
-0.8

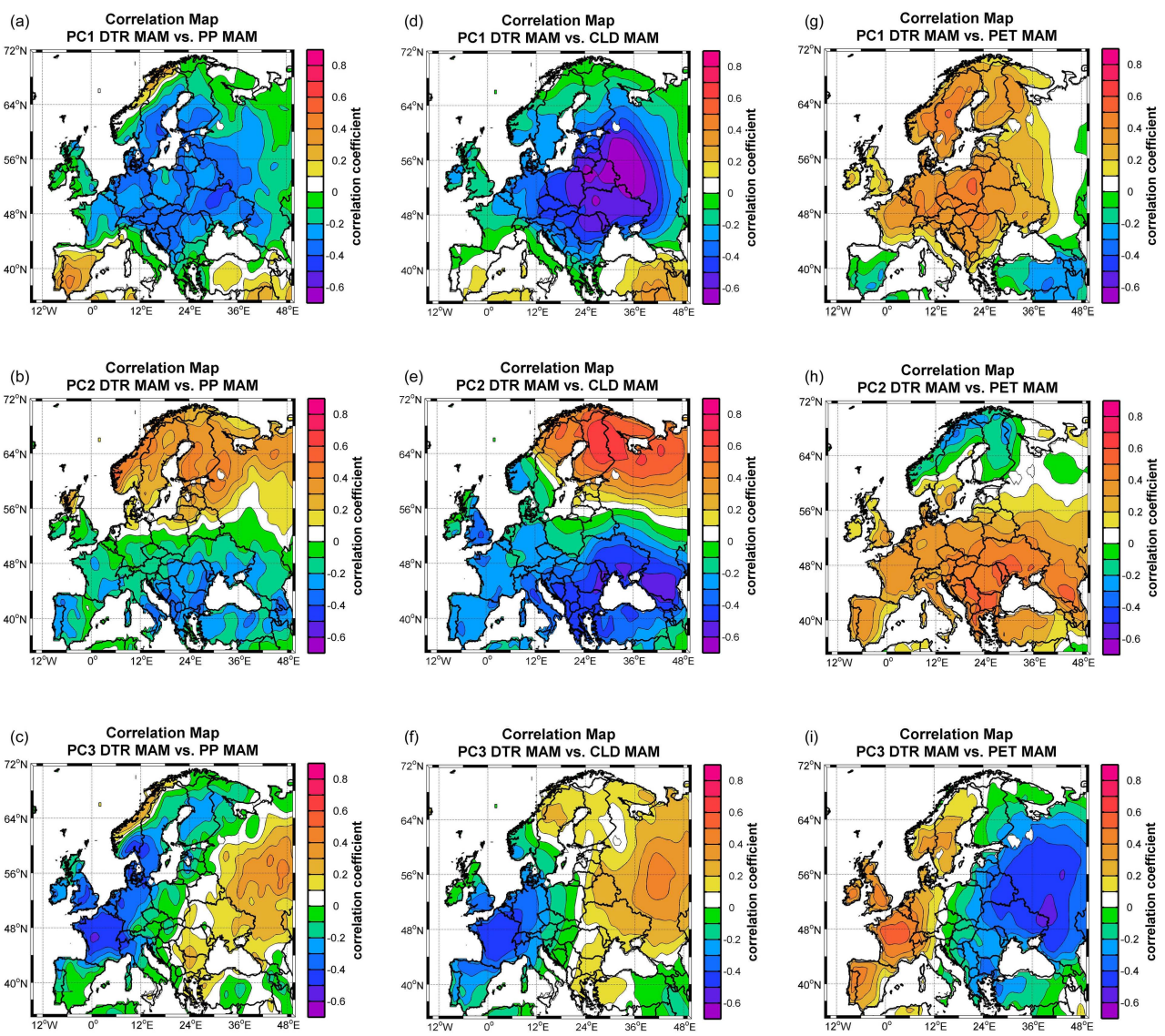
(a)
Correlation Map
PC1 DTR MAM vs. PP MAM
(b)
Correlation Map
PC2 DTR MAM vs. PP MAM
(c)
Correlation Map
PC3 DTR MAM vs. PP MAM
(d)
Correlation Map
PC1 DTR MAM vs. CLD MAM
(e)
Correlation Map
PC2 DTR MAM vs. CLD MAM
(f)
Correlation Map
PC3 DTR MAM vs. CLD MAM
(g)
Correlation Map
PC1 DTR MAM vs. PET MAM
(h)
Correlation Map
PC2 DTR MAM vs. PET MAM
(i)
Correlation Map
PC3 DTR MAM vs. PET MAM
72°N
64°N
56°N
48°N
40°N
12°W
0°
12°E
24°E
36°E
48°E
correlation coefficient
0.8
0.6
0.4
0.2
0
-0.2
-0.4
-0.6

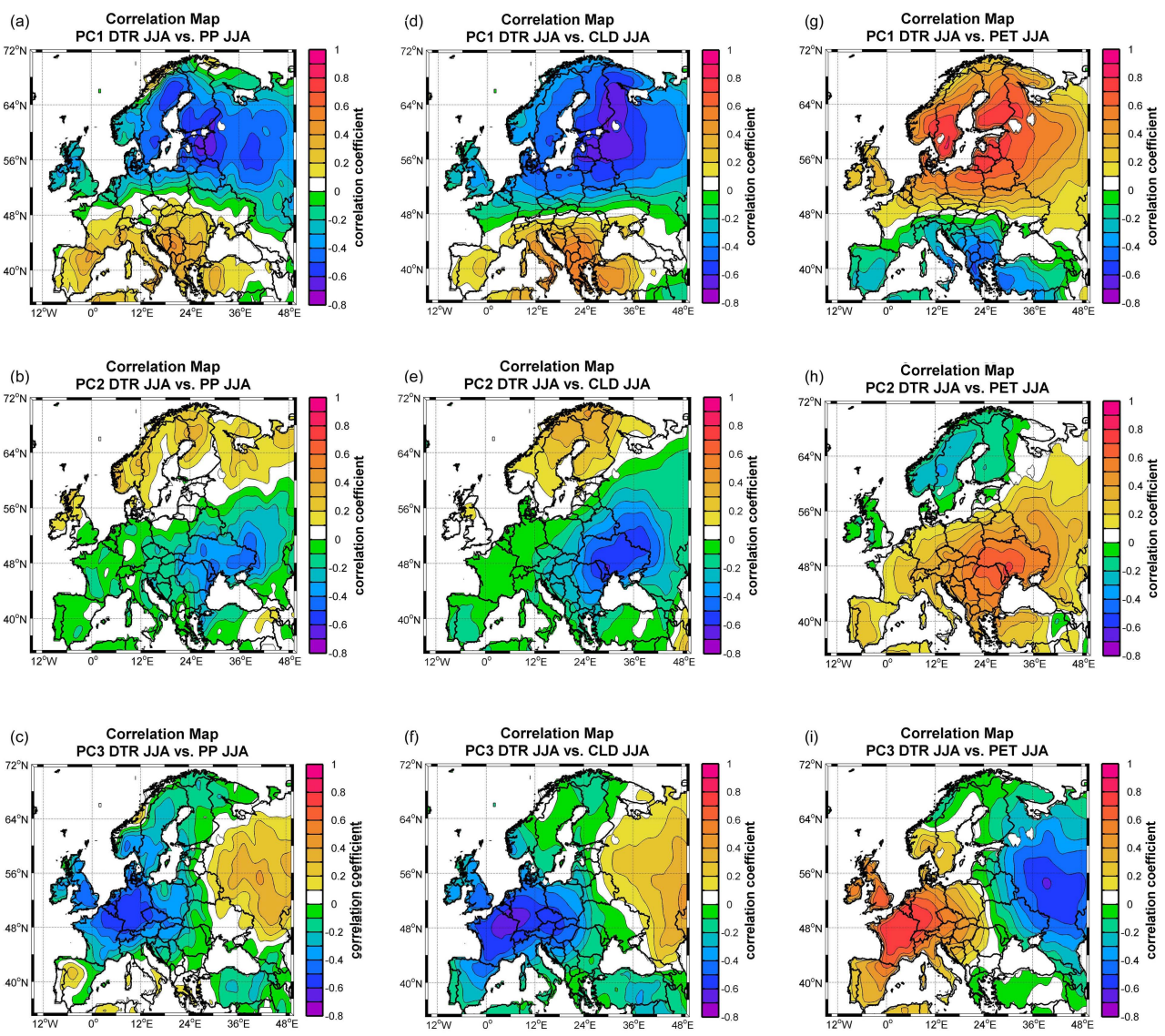
(a)
Correlation Map
PC1 DTR JJA vs. PP JJA
(b)
Correlation Map
PC2 DTR JJA vs. PP JJA
(c)
Correlation Map
PC3 DTR JJA vs. PP JJA
(d)
Correlation Map
PC1 DTR JJA vs. CLD JJA
(e)
Correlation Map
PC2 DTR JJA vs. CLD JJA
(f)
Correlation Map
PC3 DTR JJA vs. CLD JJA
(g)
Correlation Map
PC1 DTR JJA vs. PET JJA
(h)
Correlation Map
PC2 DTR JJA vs. PET JJA
(i)
Correlation Map
PC3 DTR JJA vs. PET JJA
72°N
64°N
56°N
48°N
40°N
12°W
0°
12°E
24°E
36°E
48°E
correlation coefficient
1
0.8
0.6
0.4
0.2
0
-0.2
-0.4
-0.6
-0.8

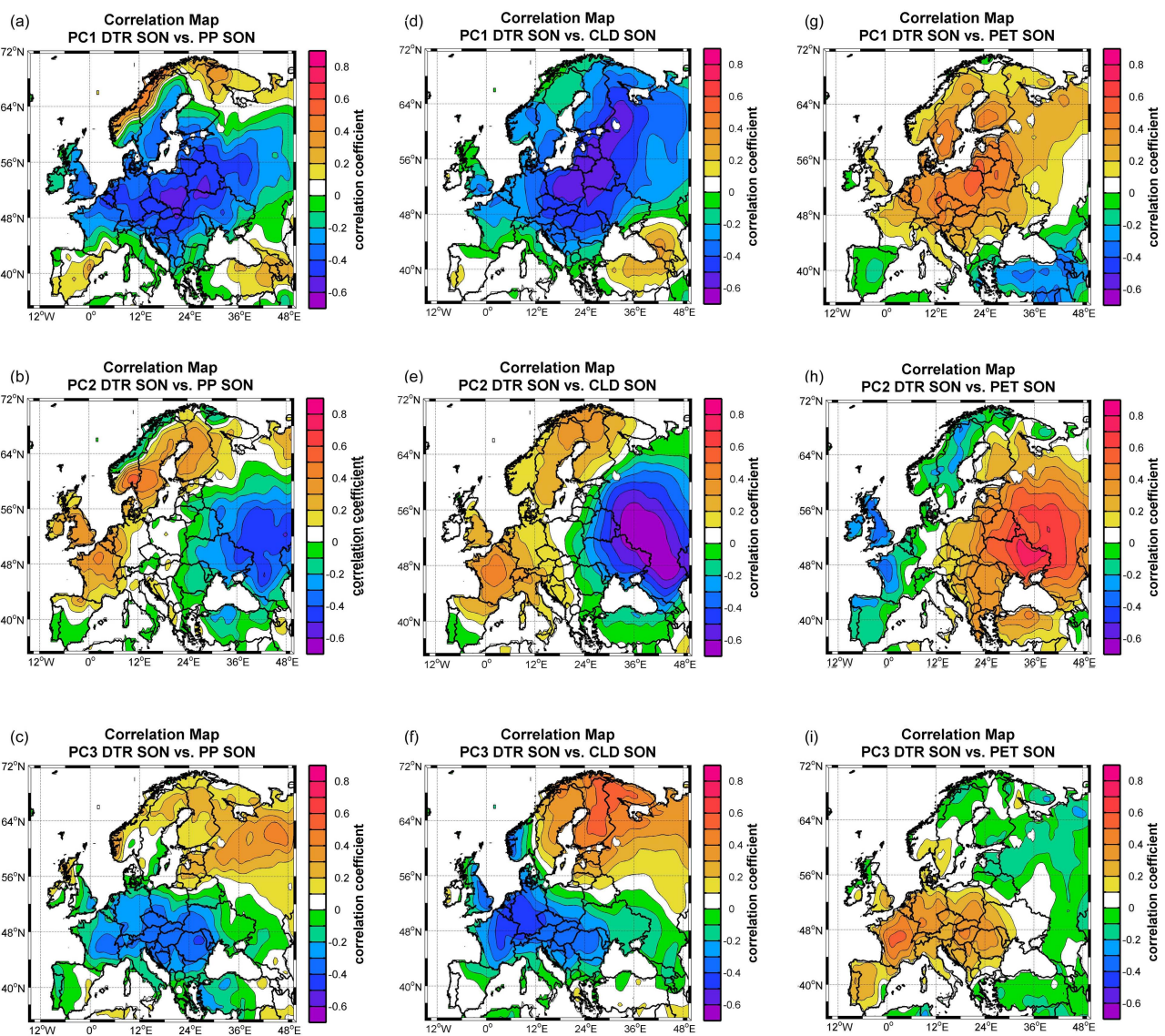
(a)
Correlation Map
PC1 DTR SON vs. PP SON
(b)
Correlation Map
PC2 DTR SON vs. PP SON
(c)
Correlation Map
PC3 DTR SON vs. PP SON
(d)
Correlation Map
PC1 DTR SON vs. CLD SON
(e)
Correlation Map
PC2 DTR SON vs. CLD SON
(f)
Correlation Map
PC3 DTR SON vs. CLD SON
(g)
Correlation Map
PC1 DTR SON vs. PET SON
(h)
Correlation Map
PC2 DTR SON vs. PET SON
(i)
Correlation Map
PC3 DTR SON vs. PET SON
72°N
64°N
56°N
48°N
40°N
12°W
0°
12°E
24°E
36°E
48°E
correlation coefficient
0.8
0.6
0.4
0.2
0
-0.2
-0.4
-0.6